The Entrainment Efficiency of Persistent Arctic Mixed-Phase Clouds as Inferred from Daily Large-Eddy Simulations during the MOSAiC Drift

Roel A. J. Neggers,[a] Jan Chylik,[a,b,c] and Niklas Schnierstein[a]

[a] Faculty of Mathematics and Natural Sciences, Institute for Geophysics and Meteorology, University of Cologne, Cologne, Germany
[b] Department of Meteorology, University of Reading, Reading, United Kingdom
[c] Department of Biology, Norwegian University of Science and Technology, Trondheim, Norway

ABSTRACT: Low-level mixed-phase clouds occur frequently and persistently in the central Arctic and thus play a key role in climate feedback mechanisms, airmass transformations, and sea ice melt. Turbulent entrainment at cloud top driven by radiative cooling modulates these clouds by affecting the boundary layer heat budget. However, reliable measurements of this small-scale process are scarce. This study presents new insights into entrainment in radiatively driven cloudy mixed layers at high latitudes based on a library of daily large-eddy simulations covering the full Multidisciplinary Drifting Observatory for the Study of Arctic Climate (MOSAiC) drift. The simulations are based on measurements, cover a periodic and homogeneously forced small domain representing conditions observed at the Polarstern research vessel, and resolve Arctic turbulence and clouds to a high degree. Approximately 1 out of 3 simulated days contains cloud mass in the liquid phase. A drift-average heat budget analysis shows that the bulk cloud-topped mixed layer is dominated by radiative cooling. Warming by top entrainment partially counters this cooling, at efficiencies of about 21%. While this compensation is significant, such efficiencies are also much lower compared to previous findings for subtropical warm marine stratocumulus. Interestingly, a few outlying MOSAiC cases show similarly high efficiencies. Analysis of turbulence energetics and dedicated sensitivity experiments reveals that high entrainment efficiency can be achieved in two ways: surface coupling and strong local wind shear. The former explains the high efficiencies in the subtropics, while the latter drives the highest efficiencies encountered during MOSAiC. In general, these findings emphasize the important role played by wind shear in boosting entrainment efficiency.

SIGNIFICANCE STATEMENT: Stratocumulus cloud layers in the high Arctic often contain liquid water at subzero temperatures. Such cloud layers cool rapidly through radiation, a process that locally creates turbulence. This turbulence causes mixing in the atmosphere. Using many high-resolution atmospheric model simulations on a supercomputer, we investigate how this mixing process causes warming in the cloud layer. The simulations are closely based on measurements made during the recent yearlong Multidisciplinary Drifting Observatory for the Study of Arctic Climate (MOSAiC) drift experiment. We find that the warming only partially counteracts the radiative cooling and that a strong change in the wind with height can affect this balance.

1. Introduction

Turbulent mixed layers and associated mixed-phase clouds are understood to play an important role in the Arctic climate system. They affect various feedback mechanisms underlying the ongoing rapid warming or amplification of the Arctic climate (e.g., Serreze and Barry 2011; Wendisch et al. 2019; Rantanen et al. 2022). In the atmosphere, they impact the vertical thermodynamic structure, the heat and moisture budgets, and the radiative budget (e.g., Morrison et al. 2012). These impacts also play a role in the air–surface interaction, through the surface energy budget (Persson et al. 2002). The cryosphere is particularly affected by liquid cloud mass boosting the downward longwave radiation at the surface, contributing to the seasonal melt of sea ice (Bennartz et al. 2013). Despite these known impacts, many aspects of cloudy mixed layers are still poorly understood. This knowledge gap is complicating their representation in larger-scale circulation models for weather forecasting and climate simulation (e.g., Tjernström et al. 2021; Day et al. 2024; Solomon et al. 2023).

One of the aspects of mixed layers that is arguably least understood is *turbulent entrainment* or the encapsulation of free-tropospheric air into the mixed layer below (see Mellado 2017 for a recent review). This mixing process at the capping inversion is driven by turbulence, which in turn is fueled by buoyant or mechanical (shear) processes. Entrainment is a classic problem in boundary layer meteorology and has been intensively researched in the past for warm (Lilly 1968) as well as cold (Curry 1986) clouds. Mixed layers at high latitudes are often decoupled from the surface (e.g., Curry et al. 1988; Tjernström and Graversen 2009; Brooks et al. 2017), with turbulence thought to be predominantly driven by radiative cooling at the top of liquid cloud layers (Curry 1986). Measuring entrainment in the Arctic is notoriously difficult, given the small scale of the associated turbulence, the delicate stability structure of Arctic inversions (Sedlar and Tjernström 2009;

Corresponding author: Roel Neggers, neggers@meteo.uni-koeln.de

Sedlar et al. 2012), and logistical challenges to operate instrumentation. Despite these difficulties, a few recent observational studies have successfully measured Arctic entrainment using airborne instrumentation (e.g., Egerer et al. 2021).

A basic understanding exists of how turbulent entrainment affects the mixed-layer heat and moisture budgets. Entrained air is typically warmer than the mixed layer, representing a heating tendency. At lower latitudes, the entrained free-tropospheric air is typically drier (e.g., Nicholls and Leighton 1986; Stevens et al. 2003); in contrast, in the Arctic, the entrained air is frequently more humid, as part of a humidity inversion (Curry 1986; Devasthale et al. 2011; Naakka et al. 2018). In the latter, the entrainment flux becomes a source term in the mixed-layer humidity budget, prolonging cloud lifetimes (Solomon et al. 2011, 2014). While the sign of these tendencies is thus set by the jumps in thermodynamic state across the capping inversion, the intensity of entrainment itself modulates these impacts. In the Arctic, the tendencies associated with entrainment are speculated to affect the transformation of air masses that enter the Arctic from lower latitudes (Pithan et al. 2018). How these tendencies structurally compare to other players in the heat and moisture budget of the lower atmosphere is still unclear.

A useful paradigm for expressing the relative importance of entrainment heating is the *entrainment efficiency* α, defined by Stevens et al. (2005) as the ratio of the entrainment heat flux at mixed-layer top E_h to the net longwave radiative flux jump across the radiatively active cloud layer $|\Delta F_{\text{rad}}|$:

$$\alpha = \frac{E_h}{|\Delta F_{\text{rad}}|}. \tag{1}$$

In this definition, efficiency α can be interpreted as the effectiveness of cloud longwave radiative cooling in driving turbulence at an inversion and thus entrainment. The critical value $\alpha = 1$ expresses parity between radiative cooling and entrainment warming, implying a balanced mixed-layer heat budget in the absence of any other tendency. Because of the denominator, this definition of efficiency is thus most applicable to turbulent cloud systems predominantly driven by radiative cooling. Efficiency α is hard to measure, and previous studies have exclusively relied on large-eddy simulation (LES). Based on LES results for coupled nocturnal stratocumulus in the subtropics, Stevens et al. (2005) found efficiencies slightly larger than 1, at which entrainment heating more than completely offsets the radiative cooling. A weak dependence on the degree of internal decoupling in the mixed layer was reported, suggesting that the turbulent transport from below plays a role in maintaining high efficiencies of entrainment at the inversion. Note that definition (1) does not account for shortwave (SW) warming at cloud top, which could be relevant for daytime cases.

One wonders if these efficiencies similarly apply to cold Arctic clouds. A first glimpse was provided by Chylik et al. (2023), who reported much lower entrainment efficiencies of about $\alpha = 0.3$ based on simulations of marine-mixed-phase convective clouds in the Fram Strait. Aerosol was found to slightly boost entrainment efficiency by a few percent. While these results suggest that entrainment warming fails to fully counteract radiative cooling in this case, it reflects only a single meteorological situation at a single location. How

representative these low efficiencies are for the wider region and other weather conditions, in particular in the central Arctic, is still an open research question.

The recent Multidisciplinary Drifting Observatory for the Study of Arctic Climate (MOSAiC) drift experiment (Shupe et al. 2020) has provided a wealth of data covering the full annual cycle (Shupe et al. 2022; Nicolaus et al. 2022; Rabe et al. 2022) that creates new opportunities for gaining insight. In a recent study, Schnierstein et al. (2024b) performed daily LESs of the Arctic boundary layer that were closely based on MOSAiC data, creating a library of close to two hundred daily cases covering the complete drift period. Surface and profiling data from the campaign were used to tightly constrain the simulations, making them representative of observed conditions. The high spatial and temporal resolutions adopted mostly resolve the turbulence and clouds in the simulations. The simulation library includes many situations that feature cloudy mixed layers, making the LES library ideal for investigating entrainment efficiency under a broad range of meteorological conditions.

The main objective of this study is to use this library of daily LES realizations for the full MOSAiC drift to assess, in a statistically significant way, what is the entrainment efficiency of radiatively driven cloudy mixed layers (RCMLs) in the Arctic. An algorithm is developed to systematically identify all RCML cases, and all variables needed to calculate entrainment efficiency are sampled from the model output. First, the statistics of all sampled RCML will be assessed, as well as the energy fluxes and tendencies that make up the energy budget. Then, the entrainment efficiency of all RCML will be investigated, not only by documenting its intensity for the full drift but also by searching for what factors control its amplitude and variation across the simulated cases. LES results for additional prototype RCML cases from different climate regimes are included in the analysis, to broaden the parameter space of atmospheric conditions and to facilitate the identification of generally applicable dependencies. Note that preliminary results of this analysis of entrainment efficiency from LES for MOSAiC were presented by Linke et al. (2023), which were still based on a simplified mixed-layer detection algorithm. This study aims to refine these early results and provide a deeper interpretation of their meaning.

Section 2 describes the data, model simulations, and analysis method in detail. Results are presented in section 3, featuring a statistical summary of defining RCML characteristics, an investigation of its drift-average bulk energy budget, the documentation of the entrainment efficiency for the full drift, an assessment of the turbulent energetics in the RCML, and the analysis of sensitivity experiments designed to test various hypotheses based on the obtained results. Section 4 discusses the findings in general, while section 5 provides concluding remarks and an outlook on future research.

2. Data and method

a. MOSAiC data

MOSAiC took place from September 2019 to October 2020, during which the Polarstern research vessel (RV) drifted with the sea ice and crossed the central Arctic during polar winter.

TABLE 1. Summary of all LES experiments featuring in this study, including a reference to the paper describing the setup. The discretization reflects the model resolution at the lowest model level. For MOSAiC, the total number of valid RCML cases is also indicated, between brackets.

Case	Reference	Number	Discretization (m)	Grid size	Sampling period (min)
MOSAiC 1100 UTC	Schnierstein et al. (2024b)	190 (58)	$20 \times 20 \times 10$	$320 \times 320 \times 286$	60–180
DYCOMS2 RF02	Ackerman et al. (2009)	1	$25 \times 25 \times 10$	$128 \times 128 \times 160$	120–360
DYCOMS2 RF01	Stevens et al. (2005)	1	$35 \times 35 \times 10$	$256 \times 256 \times 236$	120–360
CGILS S11	Zhang et al. (2013)	1	$20 \times 20 \times 10$	$256 \times 256 \times 236$	480–720
CGILS S12	Zhang et al. (2013)	1	$20 \times 20 \times 10$	$256 \times 256 \times 236$	480–720
MPACE-B	Klein et al. (2009)	1	$20 \times 20 \times 10$	$256 \times 256 \times 236$	120–300

An entire annual cycle was thus covered with continuous, state-of-the-art measurements of the atmosphere, sea ice, and ocean. Apart from permanently operated instrumentation on the ship and the sea ice, aerial platforms were deployed on days of interest. The wealth of data thus collected fills a previously existing critical data gap in Arctic science and is by now available to the science community (Shupe et al. 2022; Nicolaus et al. 2022; Rabe et al. 2022).

b. Large-eddy simulations

The LES experiments analyzed in this study all represent cases of well-mixed layers that contain liquid cloud condensate (and possibly also ice phase) and in which turbulence is at least partially generated by longwave (LW) radiative cooling at cloud top. These systems are here referred to as RCMLs. Details of all simulated cases and experiments are listed in Table 1. In all cases, the RCML is truly well mixed, without internal decoupling. Two sets of cases are included.

The first set reflects conditions as observed during the MOSAiC drift. As described in detail by Schnierstein et al. (2024b), the library includes close to 200 experiments, each for a single day, based on campaign data from the Polarstern RV and the MetCity site. The short-range (3 h) experiments are initialized at 1100 UTC, using thermodynamic profiles from the radiosonde (Dahlke et al. 2023), cloud mass profiles from the Shupe–Turner (ST) data product (Shupe et al. 2015) for the MOSAiC drift, and idealized profiles of cloud condensation and ice nucleating particle concentrations as measured at the Polarstern RV (Koontz et al. 2020; Creamean 2022). Surface boundary conditions are based on observations (Cox et al. 2023) and include the sea ice fraction, albedo, roughness length, and skin temperature. Time-composite Lagrangian forcing is applied, consisting of 6-h time averages over Lagrangian backtrajectories in ERA5 starting at the 1100 UTC radiosonde. Prescribed horizontal advective tendencies are corrected for trajectory motion, while the large-scale subsidence profile acts on the model profiles. Cloud condensation nuclei concentrations are prognostic during the simulations, while ice nucleating particle concentrations are fixed. Statistical evaluation of the full library of simulations against independent MOSAiC datasets shows that the experiments reproduce the key features of the observed yearlong surface energy budget, near-surface meteorology, and integrated cloud properties.

The second set of LES experiments represents a selection of previously published cases of RCMLs at other locations and in other climate regimes. Most cases were part of a Model Intercomparison Project (MIP) for LES codes and can thus be considered reference or prototype cases. All cases represent subtropical, warm (i.e., fully liquid) marine stratocumulus, except for ARM Mixed-Phase Arctic Cloud Experiment (MPACE-B) which represents cold (i.e., mixed phase) stratocumulus over open water north of the ARM northern slope of Alaska (NSA) site. A shared feature of all prototype RCML cases is that they are surface coupled. The exact case design and experimental setup as published are adopted here, the exception being the use of interactive surface latent and sensible heat fluxes, except for MPACE-B. The main goal of including the prototype cases is to provide context to the MOSAiC results, by linking to previous studies of entrainment efficiency and expanding the range of meteorological conditions across which this process is investigated.

All cases are simulated with the Dutch Atmospheric Large-Eddy Simulation (DALES) code (Heus et al. 2010). The general model setup described in detail by Schnierstein et al. (2024b) is applied to all cases, and only a brief summary is provided here. Resolved transport is represented using a fifth-order advection scheme, while unresolved transport is represented using a subfilter-scale turbulent kinetic energy (SFS-TKE) model. For cloud microphysics, a double-moment mixed-phase scheme is applied that features five hydrometeor species (Seifert and Beheng 2006), the implementation of which has been thoroughly tested against datasets from various recent field campaigns (Neggers et al. 2019; Egerer et al. 2021; Chylik et al. 2023; Schnierstein et al. 2024b). Clouds are interactive with radiation and aerosol. Cloud condensation nuclei are prognostic, whereas ice nucleating particle activation spectra are fixed, with concentrations of both constrained by in situ observations when available. Primary ice production consists of immersion freezing and contact freezing, dependent on temperature and cloud droplet size spectra, and nucleation deposition. The radiative transfer scheme computes optical properties of the clouds based on the size distribution of the various types of hydrometeors in the model. A dampening layer is included in the top quarter of the domain to remove spurious waves near the model ceiling. The sampling time of the experiments varies per case but is always long enough to cover significant deepening of the RCML, to allow for a robust sampling of the associated entrainment rate. The first hour of the simulation is always excluded to avoid artificial spinup effects.

c. Analysis method

A dedicated algorithm is adopted in this study to diagnose and investigate the entrainment efficiency of Arctic RCMLs.
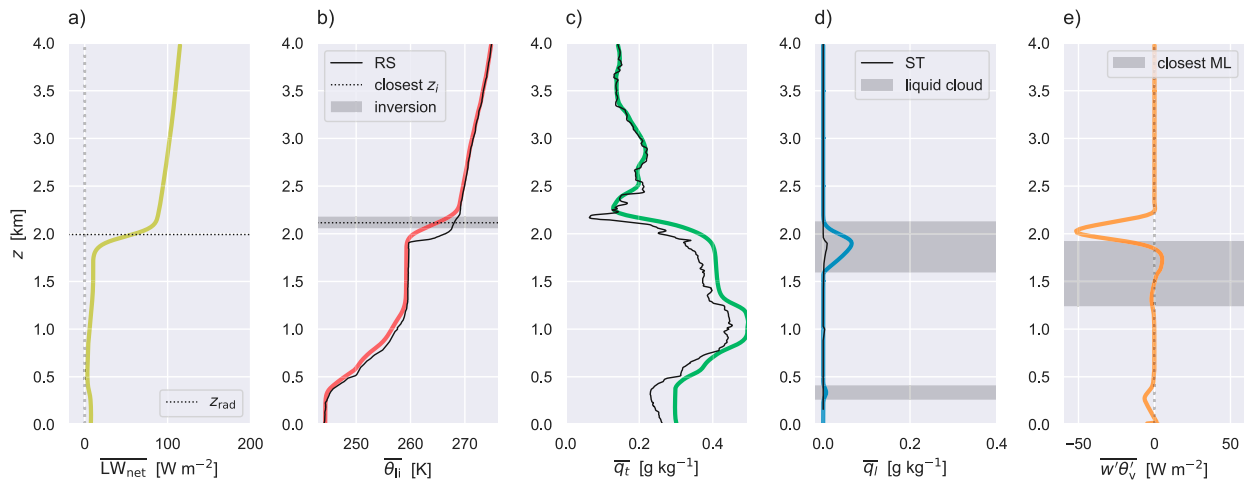
FIG. 1. Domain-averaged profiles diagnosed from the LES experiment for 7 Mar 2020 around 1100 UTC during MOSAiC, featuring a double mixed-phase cloud layer system in the lowest 3 km. (a) Net LW radiative flux LW_{net}, (b) liquid-ice water potential temperature θ_{li}, (c) total water specific humidity q_t, (d) liquid water specific humidity q_l, and (e) virtual potential temperature flux $\overline{w'\theta_v'}$. Overbars represent (horizontal) domain and time averages. In the second and third panels, the profile data from the 1100 UTC radiosonde (RS) launched at Polarstern RV are also shown, while (d) includes liquid water content (LWC) from the ST cloud product. Horizontal dashed lines and gray shading indicate various levels and layers, respectively, as detected by the algorithm and as explained in the text.

The procedure makes use of profile and time-series output from the LES model. The profile data represent horizontal averages over the simulated domain, sampled every 60 s and output as time averages every 300 s. Model output on higher moments of turbulence can be considered resolved at the applied discretizations.

1) MIXED-LAYER DETECTION

The main objective of this step is to identify the dominant RCML in an arbitrary atmospheric profile. A potential problem to be solved is that a profile can contain multiple mixed layers, some of which might not feature a strong longwave radiative flux jump. The latter can occur when (i) a mixed layer does not contain liquid cloud (Miller et al. 2015) or (ii) it is situated below other radiatively active cloud layers which dampen the net longwave cooling in the ones below (Sedlar and Shupe 2014). To address this problem, the first decision is to only consider profiles that include liquid cloud layers and that also feature a significant net longwave flux jump. Figure 1 illustrates these features for an example case of a double mixed layer, as observed at the Polarstern RV on 7 March 2020 during the MOSAiC drift.

For the profiles that meet this criterion, the following algorithm is designed to identify the dominant RCML:

(i) Identify the height of the strongest gradient in the net LW radiative flux z_{rad} (Fig. 1a).

(ii) Identify the heights of the five strongest gradients in the liquid-ice water potential temperature profile $\overline{\theta_{li}}$, here named $z_{\theta_{li}}^n$ with $n \in \{1, 2, \ldots, 5\}$, in decreasing order of strength.

(iii) For each inversion, scan the associated inversion depth using the closest local minimum and maximum of second

derivative $\partial_z^2 \overline{\theta_{li}}$ as its boundaries (Fig. 1b). Inversion layers directly adjacent to previously scanned ones are discarded.

(iv) Identify the thermal inversion $z_{\theta_{li}}^n$ that is closest to z_{rad} and define this as the thermal inversion height z_i (Fig. 1b).

(v) Perform a downward scan from the thermal inversion base z_{ib} to find the closest mixed layer, defined by the lapse rate $\partial_z \overline{\theta_{li}}$ not exceeding a threshold value (Fig. 1e).

(vi) Finally, identify the liquid cloud layer with its top closest to z_{rad} (Fig. 1d).

In practice, the algorithm is applied at every model output time step (300 s). The various vertical gradients used in steps (ii), (iii), and (v) are calculated using centered differences. A schematic overview of all heights detected by the algorithm is shown in Fig. 2.

All thresholds applied in the algorithm are listed in Table 2. Some of these values are based on previous literature, such as the static stability criterion defining the vertical extent of the mixed layer (Solomon et al. 2014) and the definition of liquid cloud layers in LES models (e.g., van Laar et al. 2019). Note that the mixed layer and inversion layer defined this way can be slightly disconnected, which has to be taken into account when diagnosing the bulk ABL heat budget, as described below in section 2c(2). Other thresholds are introduced to exclude particular days from the entrainment analysis. This happens in case (i) liquid water path (LWP) is negligible, (ii) z_{rad} is too far separated from the closest z_i and/or the top of the closest liquid cloud layer z_{ct}, and (iii) the time evolution of the selected inversion height z_i is discontinuous between output time steps. A height-separation threshold of 200 m is applied to this purpose.

Figure 3 provides further information about various heights detected by the algorithm and motivates how the height z_h for sampling the entrainment flux is set. Data points represent
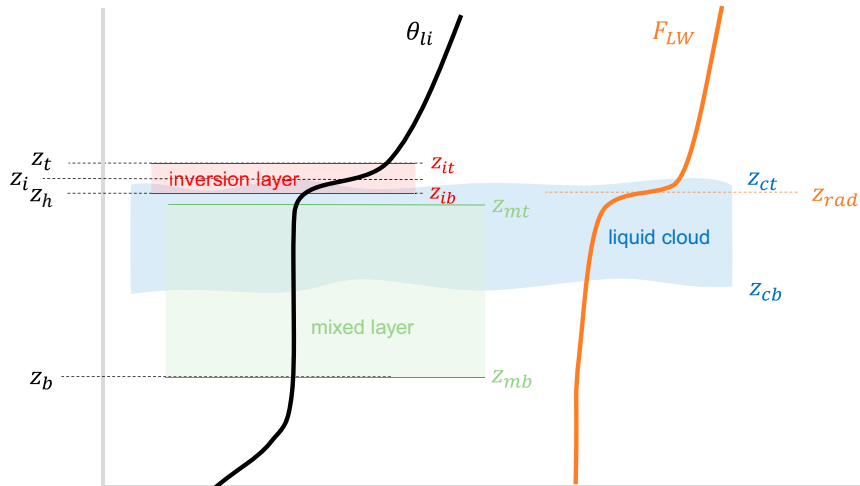
FIG. 2. Schematic overview of all heights detected by the RCML identification algorithm described in section 2c(1) (colored fonts), as explained in the text. The ML between z_{mb} and z_{mt} is indicated in green, the inversion layer between z_{ib} and z_{it} is indicated in red, and the cloud layer between z_{cb} and z_{ct} is indicated in blue. The profiles of liquid-ice water potential temperature θ_{li} (black) and net LW radiative flux F_{LW} (orange) are also shown. The heights in black font on the left are the ones adopted for calculating bulk mixed-layer properties, inversion fluxes, and inversion jumps.

time-averaged results for all valid RCML cases simulated for MOSAiC. The left panel shows the difference between z_i and the two heights that define the inversion base and top z_{ib} and z_{it}, defined in this study by the local peaks in the second derivative of $\overline{\theta_{li}}$. Also shown is the top of the mixed layer z_{ml}. The z_i is typically situated in the middle of the inversion, while z_{mt} is robustly situated somewhat below z_{ib}, the inversion base. The middle and right panels show z_{rad} and $z_{w\theta_l}$, the heights of the strongest radiative flux gradient and the minimum $z_{w\theta_l}$ flux, respectively. These two heights are typically situated close to z_{ib} and are the heights at which the entrainment flux should be sampled (to capture the strongest downward heat flux into the RCML). Note that $z_{w\theta_l}$ contains some spurious outliers situated below z_{mt} (see Fig. 3c), which reflect subsampling effects of the turbulent flux profile due to the still limited LES domain size. To avoid those in practice, we adopt z_{ib} as a more robust proxy for the minimum flux level, and it is here defined as the height z_h at which entrainment heat flux E_h will be diagnosed. This approach thus aligns with previously proposed flux-based methods for defining boundary layer heights.

TABLE 2. Overview of thresholds used in the algorithm to detect the RCML, as described in section 2c(1).

Variable	Condition	Threshold function
$\lvert z_i - z_{rad}\rvert$	<200 m	Proximity guarantee
$\lvert z_i - z_{ct}\rvert$	<200 m	Proximity guarantee
$\int \lvert \partial_t z_i \rvert dt$	<200 m	Continuity guarantee
$\lvert \partial_z \theta_{li}\rvert$	<0.005 K m^{-1}	Mixed-layer detection
q_l	>10^{-6} kg kg^{-1}	Liquid cloud detection
LWP	>1 g m^{-2}	Case inclusion

The algorithm ensures that the RCML selected for further analysis (i) contains sufficient liquid cloud mass, (ii) is likely to be radiatively driven by cloud-top cooling, and (iii) is capped by a well-defined thermal inversion. These features are key for investigating the process of radiatively driven turbulent entrainment in such layers. Scanning across potentially multiple thermal inversions in the profile makes the algorithm applicable to complex multi-mixed-layer situations and avoids including inversions that are not radiatively driven. The algorithm is in principle applicable to both model output and observational data (if available) and is capable of detecting RCMLs that are both coupled and decoupled from the surface.

Appendix A illustrates the working of the algorithm for the example day documented by Fig. 1. The topmost mixed layer is correctly selected for this case because its inversion is within the accepted proximity range to z_{rad}, as is the cloud layer top. Applying this algorithm to the full library of 191 LES cases for the MOSAiC drift yields 58 well-defined RCML cases. Ten further cases in which liquid cloud mass is present were not included in the analysis because one of the conditions listed in Table 2 was not met. Figure 4 provides a detailed overview of the simulated days and their inclusion in the analysis. During two periods in May–June and August, no simulations could be performed because of gaps in the observational data record (Shupe et al. 2020).

2) ENERGY BUDGET

The next step is to define the energy fluxes relevant for calculating entrainment efficiency. To this purpose, the bulk heat budget is considered, obtained by vertically integrating the
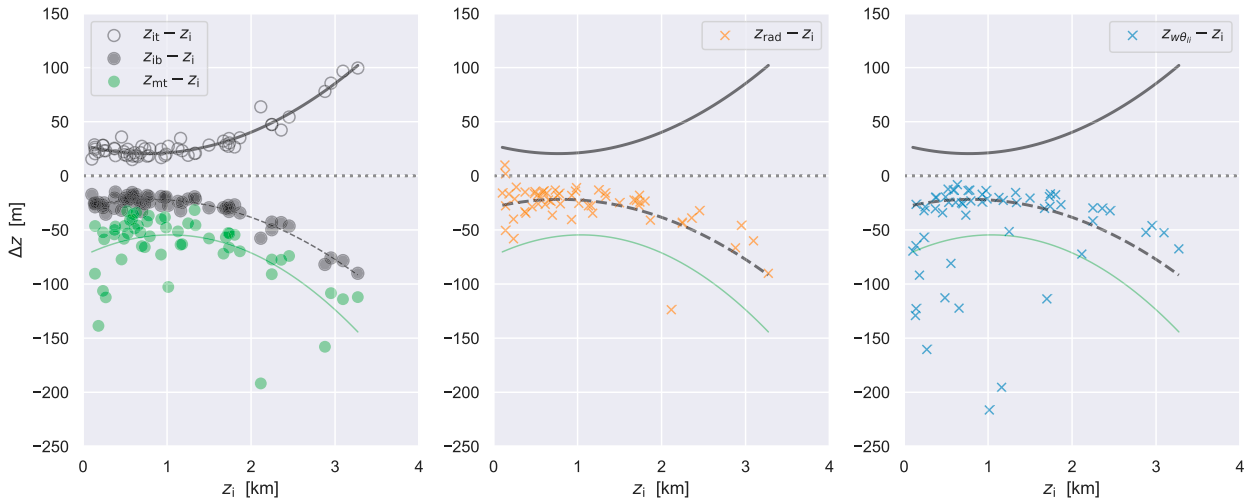
FIG. 3. Scatterplots of various heights reflecting inversion structure as detected by the algorithm described in section 2c(1). Plotted is the difference in five heights with the inversion height z_i, including (left) inversion top z_{it}, inversion base z_{ib}, mixed-layer top z_{mt}, (center) the level of strongest gradient in the radiative flux z_{rad}, and (right) the level of the strongest downward θ_{li} flux $z_{w\theta_{li}}$. Data points represent time-averaged results for all valid RCML cases simulated for MOSAiC. Second-order polynomial fits through the data in the left panel are shown in all panels, for reference.

prognostic equation for sensible heat over the layer between mixed-layer base z_b and inversion base z_h:

$$\int_{z_b}^{z_h} \rho c_p \frac{\partial \theta_{li}}{\partial t} dz = H_b + E_h + \Delta P + \Delta F_{rad} + A. \quad (2)$$

The liquid-ice water potential temperature θ_{li} is conserved for the latent heat effects of phase changes between water vapor, liquid, and frozen condensate. The term ρ is the atmospheric density, and c_p is the specific heat capacity at constant pressure. The term H_b is the upward sensible heat flux at z_b, while E_h is the downward sensible heat flux at z_h. In practice, model output of $\overline{w'\theta'_{li}}$ at those heights is used for these two energy fluxes. The term ΔP is the difference in precipitation flux across the mixed layer, with P including all falling liquid and frozen hydrometeors. The term ΔF_{rad} is the difference in the net longwave radiative flux measured across the liquid cloud layer between z_{cb} and z_{ct}. Finally, A is the vertically integrated tendency associated with the horizontal larger-scale advection of heat. Note that a subsidence term is not included in the budget, as it predominantly acts in the inversion layer which is outside the range of integration.

The entrainment efficiency can be calculated from two terms in the RCML budget in (2). The full budget puts these two terms in perspective, giving insight into how these two terms compare to those of other processes and how they contribute to the net temperature tendency of the RCML. Based on previous research of the Arctic ABL, one anticipates that the RCML should experience a net cooling rate (e.g., Curry et al. 1988). To what extent entrainment warming counteracts the radiative cooling, for the full annual cycle as sampled during the MOSAiC drift, is one of the main research questions addressed in this study.

3. Results

a. Full-drift statistics

Figure 5 presents a statistical summary of a selection of defining RCML properties as sampled from the 58 LES realizations for the MOSAiC drift. All variables reflect the state of the RCML and are relevant for interpreting the results on entrainment efficiency as presented later. The probability density functions are presented as histograms, discretized using 20 equidistant bins spanning the encountered range of values. Each case contributes one data point, representing the time average over the sampling period (60–180 min). In general, despite some scatter, distribution shapes can be recognized for all variables, suggesting the sample size of 58 RCML cases

FIG. 4. Classification table of all simulated days during MOSAiC. Days marked white are not part of the simulation library, while days with all other colors were successfully simulated. Dark blue: no liquid cloud (excluded). Gray: liquid cloud present but no valid RCML detected (excluded). Orange: liquid cloud present and valid RCML (included).
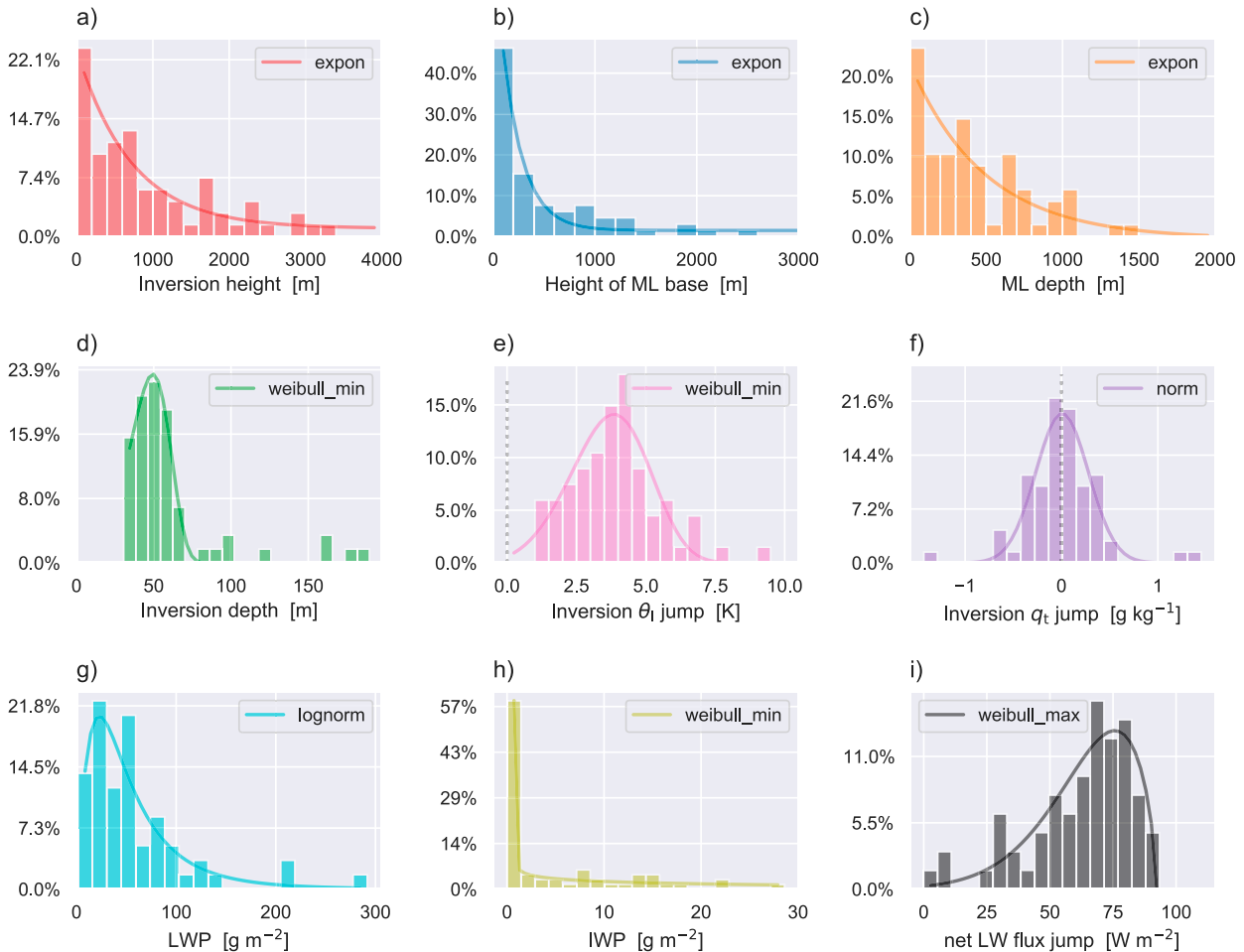
FIG. 5. The pdfs of properties of the 58 RCMLs and associated inversion and clouds as diagnosed from the LES experiments for the MOSAiC drift. (a) Inversion height z_i. (b) Height of mixed-layer base z_b. (c) Mixed-layer depth $z_h - z_b$. (d) Inversion depth $z_t - z_h$. (e) The θ_l jump across the inversion. (f) The q_t jump across the inversion. (g) LWP of the RCML cloud layer. (h) IWP up to RCML cloud top. (i) Net LW radiative flux jump across the RCML cloud layer. Data are sorted into 20 bins across the sampled range. The solid lines represent fits within this range, using the SciPy functional forms as indicated.

goes some way toward capturing typical distributions. For reference, a functional form is fitted to the centers of the bins, chosen based on either previous literature (LWP) or as inspired by the apparent shape of the probability density function (pdf).

Figure 5a shows the distribution of the thermal inversion height z_i, which is most often located within the lowest kilometer. Very few inversions are found above 3 km. The distribution seems exponential, with very low inversions being by far the most frequent. This is commensurate with the idea of stability being strongest close to the surface in the Arctic (Overland et al. 1997). Figure 5b shows the RCML base height z_b, which similarly is most frequently found close to the surface. In that sense, its distribution is similar to that of z_i, below which the RCML is per definition situated and by which it is thus constrained. The RCML base is frequently elevated, corresponding to mixed layers decoupled from the surface. Figure 5c shows the distribution of RCML depths $z_h - z_b$, expressing not only that very shallow mixed layers

dominate but also that depths of up to 1 km still occur frequently. This result expresses that relatively deep mixed layers have a significant presence in the high Arctic.

Figures 5d–f focus on the thermal inversion. Its depth $z_t - z_h$ peaks at about 50 m, which is close to but still slightly higher than the vertical discretization of the LES experiments. This means that the impacts of discretization on the lower end of this distribution cannot be excluded and expresses that high resolution is required to correctly represent Arctic inversions in models. In addition, the adopted definition of the inversion layer also affects these data. The distribution tails off above 100 m, with few occurrences above. The next two panels, Figs. 5e and 5f, show thermal inversion strengths, as expressed by the jumps in θ_l and q_t, respectively, being the prognostic variables for thermodynamic state as used in DALES. For temperature, a positive-definite and reasonably broad distribution is found, with a single well-defined mode at about +4 K and with a long tail toward higher values. The mode can be interpreted as the typical inversion strength of

the Arctic RCMLs as encountered during the MOSAiC drift. Very small jumps are not diagnosed, probably due to such inversions being obscured by other inversions in the profile. The humidity jumps (as sampled over the thermal inversion) are not positive definite but seem randomly distributed around zero, with most amplitudes found between -1 and 1 g kg^{-1}. This suggests that humidity inversions (i.e., positive jumps) occur as frequently as humidity "drops" (i.e., negative jumps). This result is relevant for interpreting the importance of such inversions in the Arctic climate, which is in line with existing climatologies of this characteristic feature of the Arctic atmosphere (Naakka et al. 2018).

The lowest row of panels (Figs. 5g–i) presents properties of clouds and radiation associated with the RCMLs. Low values of LWP occur most frequently, although the data contain too much scatter to confirm the lognormal shape as reported in previous observational studies (e.g., Huang et al. 2014; Kostsov et al. 2018; Zuidema et al. 2005). In contrast, ice water path (IWP) spikes at very small values but has a long but shallow tail toward larger values. What process shapes this distribution is unclear, but the sporadic high values could be related to cloud ice sedimenting into the RCML from higher levels (e.g., Fernández-González et al. 2015; Dedekind et al. 2024). Finally, the radiative flux jump across the RCML shows a well-defined mode at about 75 W m^{-2}, with the distribution skewed toward lower values. The mode likely reflects the LWP value at which the longwave cloud-radiative effect starts to saturate (Stephens 1978; Miller et al. 2015).

b. Bulk energy budget

Figure 6 documents the drift-averaged bulk sensible heat budget for the 58 RCMLs as simulated for MOSAiC. The data are sampled from the time- and domain-averaged simulation output, and various percentiles are calculated to indicate the median and the distribution around it. The median net radiative cooling ΔF_{rad} is 67.3 W m^{-2} and dominates the budget. As a result, a median net cooling tendency of 49.3 W m^{-2} exists, which is commensurate with the early observational studies of Curry et al. (1988) and reflects that these RCMLs are embedded in transforming air masses that are gradually cooling (e.g., Pithan et al. 2018). The entrainment heat flux at RCML top is the term with the second largest amplitude ($+14.4$ W m^{-2}) and is the sole warming term to counteract the radiative cooling. All other terms are much smaller, including the vertically integrated advection term A. The latter is due to the Lagrangian calculation of this forcing term and to the fact that the RCML is typically relatively shallow. The ratio of the median entrainment warming to the median radiative cooling is 21.5% and as defined by (1) expresses the efficiency of the entrainment process in partially counteracting the radiative cooling at cloud top that drives it. On the one hand, this means that more than 1/5 of the radiative cooling in the RCML is canceled out by entrainment, a significant fraction which should matter for the transformation of cloudy air masses in the Arctic. However, on the other hand, the efficiency expressed by this year-averaged RCML budget is also much lower than subtropical marine conditions as
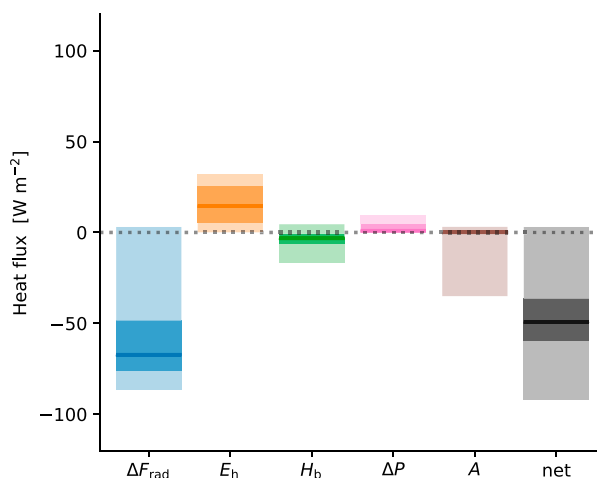

FIG. 6. Full-drift bulk mixed-layer heat budget as calculated over all 58 MOSAiC RCML cases. The abscissa labels refer to the terms as defined in section 2c, with the last column being the net tendency. For each term, the median is indicated by the thick horizontal line, and the interquartile and 5th–95th percentile ranges are indicated by medium and light shading, respectively. The term ΔF_{rad} is the difference in the net LW radiative flux measured across the liquid cloud layer. The term E_h is the downward sensible heat flux at z_h, and H_b is the upward sensible heat flux at z_b. The term ΔP is the difference in precipitation flux across the bulk layer. The term A is the vertically integrated tendency of horizontal heat advection. The term "net" is the net total tendency of all terms combined.

reported by Stevens et al. (2005) and is in line with the low values reported for an Arctic case by Chylik et al. (2023). The reason for this apparent inefficiency, including its variation during the MOSAiC drift, is investigated in more detail in the next sections.

c. Entrainment efficiency

Figure 7 shows the entrainment heat flux E_h plotted against $|\Delta F_{\text{rad}}|$ for each individual case. The MOSAiC cases form a well-defined cluster in this phase space, situated below the diagonal that represents parity between heating and cooling. This can be interpreted as "subefficient" entrainment. The spread among cases in $|\Delta F_{\text{rad}}|$ and E_h is large, as also reflected in the pdf shown in Fig. 5i. The colored dots represent the prototype cases listed in Table 1, all located at or slightly above the diagonal. This expresses "superefficiency," in that entrainment warming outweighs radiative cooling. Note that high efficiency is also found for the cold mixed-phase MPACE-B case, as well as for three outlying MOSAiC cases. These MOSAiC outliers are indicated by special markers (crosses), a notation that will also be applied in the following figures, for reference. This result seems to suggest that low temperature itself, or the presence of cloud ice, is not the prime cause for low entrainment efficiencies; however, a deeper analysis is needed to gain further insight (see section 3e).

Figure 8 quantifies the entrainment efficiency α and queries its dependence on LWP, inspired by a similar analysis by Stevens et al. (2005). Again, the MOSAiC cases are contrasted

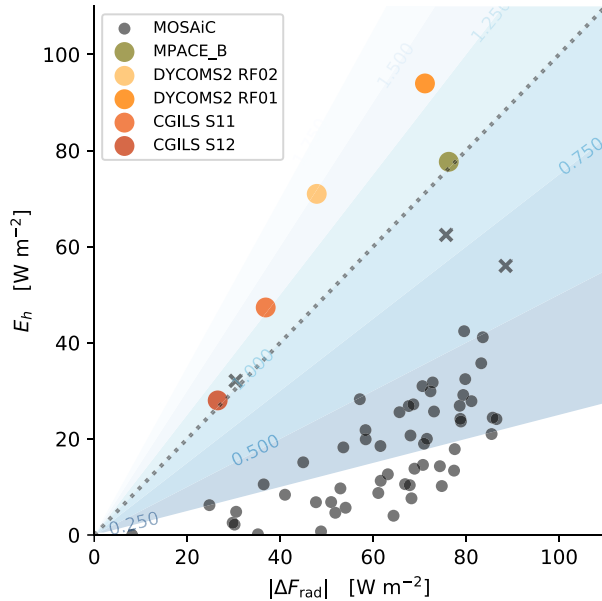FIG. 7. Scatterplot of the entrainment heat flux E_h vs the net radiative flux jump $|\Delta F_{rad}|$. Each dot represents a daily value, calculated as the average over the sampling period in the LES experiment. MOSAiC cases are shown as small gray dots, with crosses indicating the three cases with the largest entrainment efficiency α. The prototype cases are shown as bigger colored dots. Blue background shading indicates the entrainment efficiency α field, as defined by (1). The isoline $\alpha = 1$ is highlighted (black dotted diagonal). Data points above the diagonal represent superefficiency, while those below are subefficient.

to the prototype scenarios, with the high-efficiency MOSAiC outliers again highlighted. The side panels show the MOSAiC pdfs of both variables, respectively. The pdf for LWP is already shown in Fig. 5g, for reference. For MOSAiC, we find a mean entrainment efficiency of $\alpha = 0.26$, with relatively little spread. A weak dependence of efficiency α on LWP is apparent, with low efficiencies found at low water paths and saturating around the mean value from approximately LWP > 50 g m^{-2}. This is most likely related to the longwave radiative effect of liquid cloud layers saturating at around the same value.

More insight into entrainment is provided by Fig. 9, showing the relative contribution to the entrainment heat flux by the entrainment rate ϵ and the thermal inversion temperature jump $\Delta\theta_l$. Here, ϵ is derived from the mixed-layer mass budget (e.g., Stevens et al. 2003), as the residual of the tendency in z_i and the large-scale subsidence rate diagnosed at z_i (prescribed in these simulations). Lines of equal E_h (their product) are indicated by the solid gray lines. The large spread in this phase space indicates that the temperature jump and the entrainment rate can both be the main contributors to the heat flux. The MOSAiC temperature jumps tend to weakly cluster around +4 K, reflecting the mode in the pdf already shown in Fig. 5e. Interestingly, the prototype high-efficiency cases do not overly stand out in this phase space. This apparent similarity in the amplitude of entrainment heat flux E_h suggests that, for the high-efficiency cases, the RCML

turbulent system can somehow produce similar E_h values at already much smaller radiative flux jumps. Where this additional energy comes from, and what are the underlying processes, is yet unclear.

The variation of α as a function of time during the yearlong drift is shown in Fig. 10. A weak seasonal dependence is apparent, in particular in the monthly mean, with lower values occurring during Arctic winter. However, the signal is weak compared to the day-by-day variation and not statistically significant. In addition, high-efficiency outliers exist, one on 7 March 2020 and another on 7 July 2020. These outliers, also visible in Figs. 7 and 8, seem not to have a preferred season. Another possible impact on entrainment efficiency is surface coupling, here defined as the RCML base being located at the surface. Figure 10 suggests that α is not structurally higher among coupled cases during MOSAiC.

d. Turbulent energetics

Figure 7 illustrates that the high-efficiency MOSAiC cases produce a higher entrainment heat flux for a given amount of radiative cooling. This means that either (i) additional energy is available for driving turbulent entrainment or (ii) in some way the turbulence makes more efficient use of the given forcing (the radiative cooling rate). As both options concern the energetics of turbulence, it makes sense to take a closer look at TKE. This is also inspired by recent studies on the link between entrainment and TKE in warm stratocumulus-topped boundary layers (Bretherton and Blossey 2014; Kazil et al. 2017).

The first step is to probe the connection between entrainment heat flux E_h and TKE as diagnosed at the same height. Figure 11a confirms the existence of a reasonably tight relation, as expressed by a high correlation coefficient (0.90). Interestingly, the dependence explains the internal variation not only for the MOSAiC cases but also for the set of prototype cases featured in this study. The tight relation between E_h and TKE$_h$ suggests that for understanding entrainment efficiency, one needs to gain insight into how TKE is generated and/or maintained in the entrainment zone. More insight into the vertical structure of TKE in the RCML is provided by Fig. 11b. Most MOSAiC cases have a convex internal TKE structure, with a single maximum in the middle, while the prototype cases have a more concave structure, with two maxima at the RCML boundaries. The latter suggest that horizontal wind shear at those mixed-layer boundaries might play a role in boosting TKE in the prototype cases. Interestingly, some MOSAiC cases have a similar maximum in TKE near the inversion; these are also the cases with relatively large E_h (see Fig. 11a) and the largest entrainment efficiencies (see Fig. 7).

To understand those maxima near the inversion, the TKE budget is considered next. Figure 12 shows the vertical mixed-layer profiles of the buoyancy flux term B, the mechanical production term S, and the transport term T. For visualization, the two sets of cases are now plotted separately and as an ensemble composite. Also, note that the plotting range is 4 times larger for the prototype cases. For the MOSAiC cases, B tends to be weakly positive near RCML top, which is
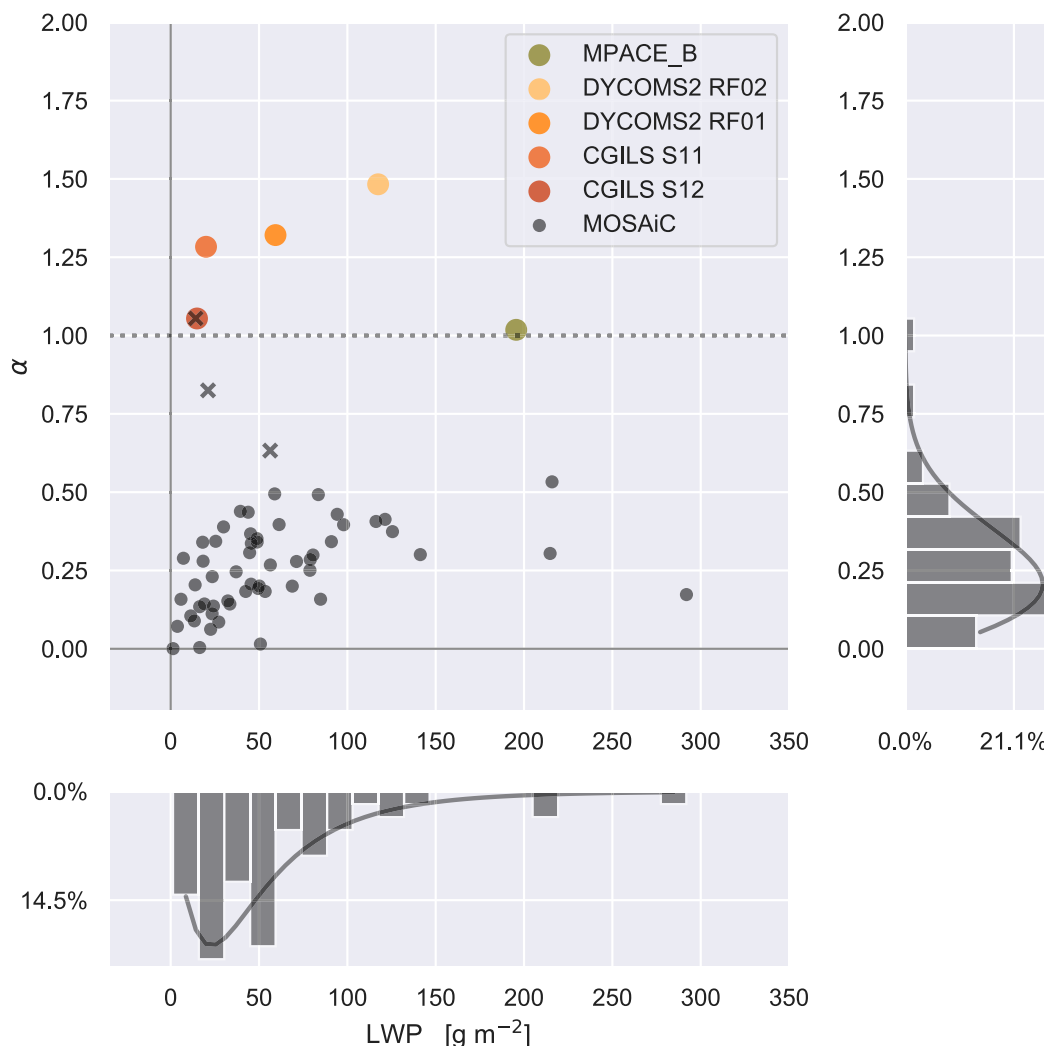
FIG. 8. As in Fig. 7, but now showing LWP vs entrainment efficiency α. The horizontal dotted line marks reference value $\alpha = 1$, at which entrainment heating balances radiative cooling. The side panels show the probability density functions of the MOSAiC simulations for both variables. Solid black lines reflect fits of the lognormal (LWP) and Weibull α functional forms to the histogram centers.

associated with the longwave radiative cooling near that height. This composite structure is similar to the buoyancy flux profile of the single case shown in Fig. 1e. Near mixed-layer base B is generally smaller in amplitude and negative. The prototype cases share the radiatively driven peak in B near mixed-layer top, being somewhat larger. However, B differs greatly further down. First, the level of minimum B is now situated near the middle of the mixed layer, not at the ML base. Second, B is relatively large and positive near mixed-layer base. This vertical structure in B is consistent with substantial surface buoyancy forcing of turbulence, accompanied by a proximity to internal decoupling in the mixed layer (Bretherton and Wyant 1997). Indeed, all prototype cases are surface coupled.

The mechanical TKE production term S has a double-peak structure for the MOSAiC cases. A small maximum exists near mixed-layer top, probably expressing local wind shear in

the thermal inversion layer. Below the local minimum, S gradually increases toward mixed-layer base again, which suggests that top-down driven cold downdrafts gradually sink from the mixed-layer top into a weakly sheared layer below. Note that S exhibits significant spread and positive skewness. While the prototype cases share the double-peak structure in S, the mode near mixed-layer base is considerably larger and much more local. This suggests that these surface-coupled cases tap into the significant potential mechanical TKE source that exists close to Earth's surface, associated with the wind reducing to zero at the surface layer height.

The transport term T finally expresses how the generated TKE is distributed across the RCML. For the MOSAiC cases, T tends to be negative where B is maximum and is weakly positive in the lower half of the RCML. This indicates that buoyancy-produced TKE in the upper part of the mixed layer is redistributed downward. For the prototype cases, the
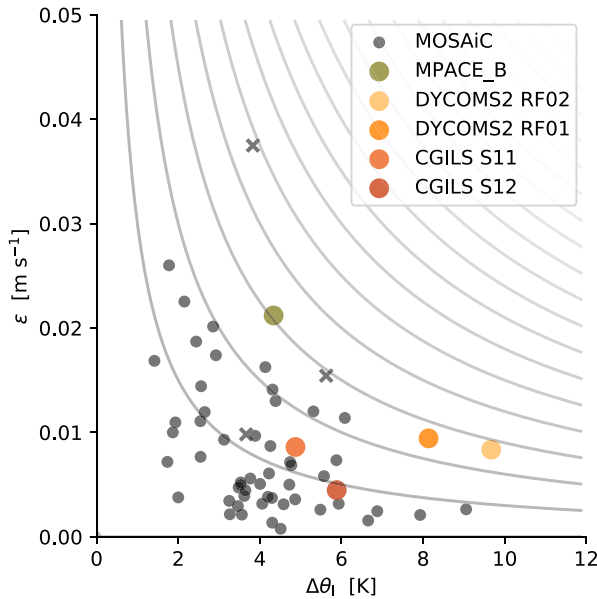
FIG. 9. Scatterplot of jump in θ_l across the thermal inversion vs the entrainment rate ϵ. Isolines of their product are shown as solid gray lines, with values increasing toward the top right.

FIG. 10. Time series of entrainment efficiency α during the year-long MOSAiC drift period. Open markers indicate days with surface-coupled RCMLs, defined here as mixed-layer base being below 30-m height. The orange line indicates the monthly mean, omitting months with less than 2 simulated days.

vertical structure of T is mirrored, featuring a well-defined negative range in the lower half of the mixed-layer base and a positive range above. In addition, the amplitude of T is notably larger compared to the MOSAiC cases. Apparently, much more TKE is moving around inside the RCML, dominated by strong bottom-up transport.

The large spread and strong skewness in S visible in Fig. 12a are investigated in more detail in Fig. 13a, showing the individual S profiles for all MOSAiC cases. A few outlying MOSAiC cases with strong mechanical TKE production are responsible for the skewness, which has much larger magnitudes than the median. These magnitudes are comparable to or even exceed those found among the trade wind prototype cases. The skewness-causing MOSAiC cases are also the cases with the largest entrainment efficiency.

Given these large differences in shear TKE production, the final step is to vertically integrate the TKE-producing budget terms over the mixed layer, up to the entrainment height (inversion base). This gives insight into how high-entrainment-efficiency cases manage to maintain such high levels of TKE. Figure 13b shows a scatterplot of the vertically integrated buoyancy term B_{int} versus the mechanical term S_{int} (term T is not considered here because its vertical integral is negligible). Only positive budget values are included in the integrals, thus focusing exclusively on TKE production. The distribution of cases apparent in this phase space can be interpreted as follows. First, total TKE can be large through strong positive buoyancy production (x axis). This is the case for most prototype cases, profiting from positive B in both the lower and upper parts of the RCML (see Fig. 12b). Second, cases can also have large TKE because of strong shear production S (y axis). This is again true for most prototype cases and then predominantly contributed by the large values of S close to the surface
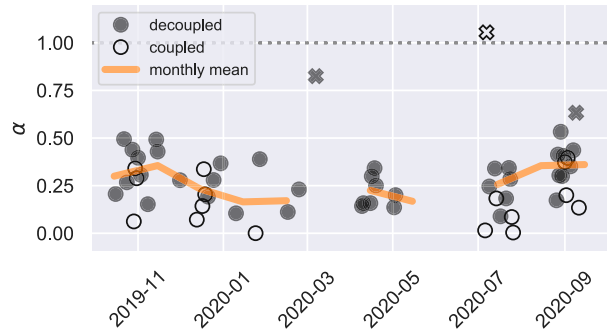
(see Fig. 12b). Interestingly, the three highest-efficiency MOSAiC cases also have the strongest integrated shear production (7 March 2020, 7 July 2020, and 9 September 2020; see Fig. 10). Shear production among those is of similar magnitude to the prototype cases and is accompanied by very weak buoyancy production.

These results suggest that both strong buoyancy production and high wind shear can boost the entrainment efficiency of RCMLs. While high entrainment efficiency among the set of MOSAiC cases is predominantly driven by strong wind shear, the prototype RCML cases all profit from a combined strong buoyancy and shear production of TKE closer to the surface boundary, to which they are coupled.

e. Hypothesis testing

A set of sensitivity LES experiments was performed to test various hypotheses coming out of the analyses above. The first test focuses on the Dynamics and Chemistry of the Marine Stratocumulus (DYCOMS2) and the high-shear 7 March 2020 MOSAiC case, first reducing shear in the wind profile and then in addition reducing the surface sensible and latent heat fluxes to zero. This should prove or disprove the hypothesis that wind shear and surface coupling boost entrainment efficiency from the baseline value of about 20% that is speculated to represent pure cloud-top cooling. Wind shear is in effect reduced by multiplying the wind profile everywhere by a factor of 0.1. Figure 14 shows that reducing shear immediately leads to a significant drop in the entrainment heat flux (and with it its efficiency) in both cases, while leaving the radiative cooling more or less unaffected. Then, in addition, switching off the surface fluxes further drops the entrainment efficiency in the trade wind case (again preserving radiative cooling) but not in the MOSAiC case. The latter is explained by the RCML already being fully decoupled from the surface. Apparently, the environmental conditions in both cases can be manipulated such that the entrainment efficiency more or less reduces to the low value typically encountered for most MOSAiC cases. In the absence of other turbulence-affecting processes, this
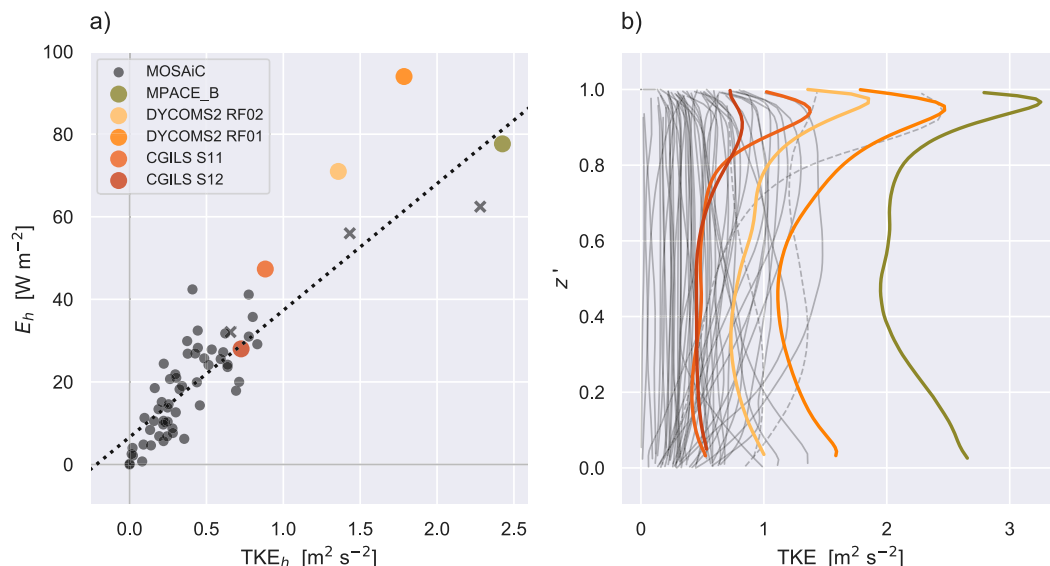
FIG. 11. (a) Scatterplot of the entrainment heat flux E_h against TKE at the same height TKE_h. The dotted black line is a linear regression over all shown data points with correlation coefficient = 0.90, slope = 34.94 W m^{-4} s^2, and intercept = 5.61 W m^{-2}. (b) Vertical profiles of TKE in the RCML. The term z' is the normalized height in the layer between z_b and z_h. The three MOSAiC cases with the highest entrainment efficiency are indicated by the dashed line style.

value can thus be considered baseline efficiency associated with purely radiatively driven entrainment.

Another sensitivity run was performed to investigate the impact of the ice phase on entrainment efficiency. For one randomly selected MOSAiC case, an LES experiment was conducted with the double-moment microphysics scheme in warm mode, meaning that only two hydrometeors, cloud liquid water and rain, were represented. The result is shown in Fig. 14. Switching off ice eliminates glaciation, which acts to increase cloud liquid water mass. This slightly increases not only the radiative cooling but also the entrainment flux, with their ratio more or less preserved. Other aspects of the RCML remain more or less unaffected. Apparently, the impact of glaciation on the entrainment efficiency is small, being second order
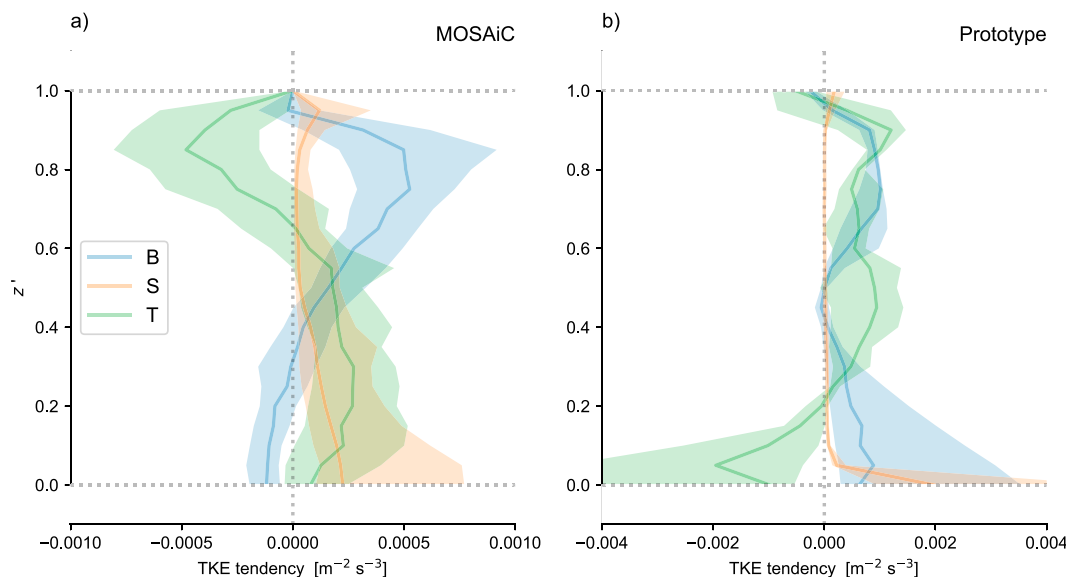

FIG. 12. Composite mixed-layer profiles of various terms in the TKE budget. (a) MOSAiC cases. (b) Prototype cases. The term z' is the normalized height in the ML. Colors represent the buoyancy flux term B (blue), the mechanical production term S (orange), and the TKE transport term T (green). Shading represents the interquartile range of the ensemble, while its median is indicated by the solid line. For visualization, a wider data range is applied on the horizontal axis in (b).
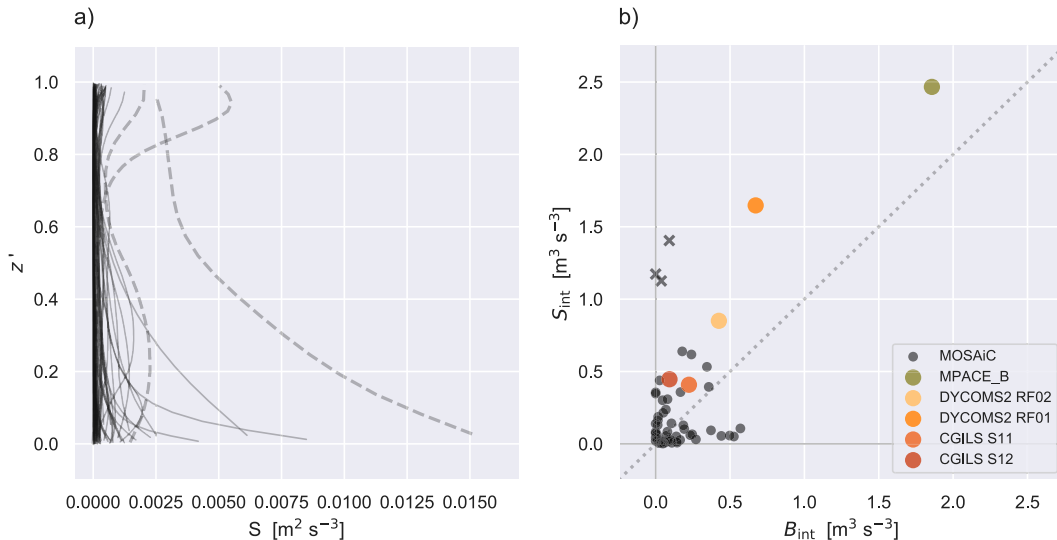
FIG. 13. (a) As in Fig. 12a, but now showing individual profiles of the mechanical production term S within the ML of all MOSAiC cases. (b) Scatterplot of the buoyancy term B vs mechanical S term as integrated over the height range $0 < z' < 1$. Only positive contributions representing TKE production are included in the integrals. The three cases with the largest entrainment efficiency α are indicated by the dashed lines in (a) and the crosses in (b). Of the 58 shown MOSAiC cases, 20 are shear dominated, here defined as $S_{int} > B_{int}$.

compared to those of shear and surface coupling (see also Fig. 15). This result could be consistent with insights from previous studies on the role of limited ice precipitation in the persistence of supercooled clouds (de Boer et al. 2011; Silber et al. 2021). However, note that at 3 h, the simulated time period is rather short; in case persistent glaciation shortens the liquid cloud life cycle and causes its eventual disappearance, the whole turbulent RCML would collapse including entrainment, and the impact would be much bigger. These potential longer-term effects of ice formation are not investigated here.

4. Discussion

The impact of wind shear on entrainment in the dry convective boundary layer has been investigated in previous studies (Mellado 2017; Haghshenas and Mellado 2019). Most studies of entrainment in cloud-topped mixed layers have not considered this impact, however, and focused on the role of buoyancy-driven turbulence (Stevens 2002). There are a few notable exceptions. Brost et al. (1982) studied the way mechanical production contributed to the turbulent variance budgets in subtropical stratocumulus cloud decks under high-wind conditions. Driedonks and Duynkerke (1989) mentioned the role of wind shear in their review of the same cloud regime. Curry et al. (1988) investigated TKE budgets for observed boundary layer clouds in the summertime Arctic, reporting significant TKE generation by shear in the inversion layer.

Defining differences between this study on entrainment and the ones mentioned above are (i) the focus on radiatively driven cloudy mixed layers at high latitudes, (ii) the use of turbulence-resolving LES based on in situ observations, (iii) coverage of the full annual cycle, not just summertime but also

including polar winter, and (iv) the large sample size of the library of cases considered, each representing unique atmospheric conditions. A key new insight is that wind shear can boost entrainment efficiency in Arctic cases, beyond that driven by radiative-cooling-induced buoyancy alone. A second important outcome is that high entrainment efficiency in subtropical cases appears at least partially driven by mechanical turbulence generation at the surface due to shear in the low-level trade wind flow. Both findings underline the importance of considering wind shear in understanding the problem of top entrainment in turbulent cloud-topped mixed layers in general.

An intriguing result that stands out is that a substantial number of MOSAiC cases, not just the three high-efficiency cases, have only weak integrated buoyancy production and seem predominantly driven by shear production (see the 20 data points above the diagonal in Fig. 13). In those shear-dominated cases, the cloud-top radiative cooling is still considerable; indeed, they all have a locally positive maximum buoyancy flux near mixed-layer top (see, e.g., Fig. 1e). We speculate that the radiative cooling plays a role in generating extra TKE in these situations by initiating turbulent perturbations within high-shear zones. This additional TKE is subsequently distributed over the mixed layer. The pressure-scrambling effect mentioned by Brost et al. (1982) could play a role in this process. Gaining further insight is a future research topic.

Contrasting Arctic with non-Arctic RCML cases was a key step in obtaining these insights. The results are perhaps best summarized by plotting entrainment efficiency for all cases against the local TKE at entrainment height normalized by the net radiative cooling, as shown in Fig. 15. The relatively tight linear dependence, as expressed by the high correlation
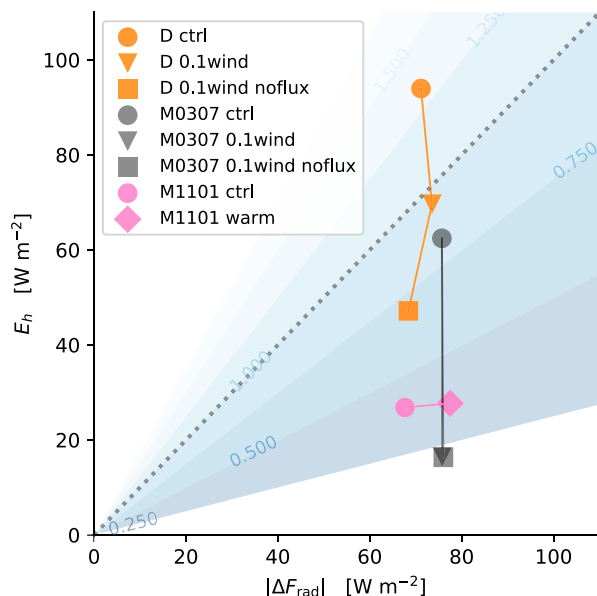
FIG. 14. As in Fig. 7, but now showing results for only three cases: DYCOMS2 RF01 ("D," orange), MOSAiC 7 Mar 2020 ("M0307," black), and MOSAiC 1 Nov 2019 ("M1101," pink). Apart from the control runs ("ctrl," circles), also included are results from various sensitivity LES runs such as experiments with reduced shear ("0.1wind," triangles), experiments with reduced shear and zero surface heat fluxes ("0.1wind noflux," squares), and an experiment without ice microphysics ("warm," diamond). Blue background shading indicates the entrainment efficiency α field, for reference (values labeled).

FIG. 15. Scatterplot of TKE at inversion base normalized by the net LW radiative flux jump $|\Delta F_{net}|$ against entrainment efficiency α. The sensitivity runs as discussed in section 3e are also included, using the same markers. The dotted black line is a linear regression through all data points, with a correlation coefficient of 0.91, slope = 38.11 W m^{-4} s^2, and intercept = 0.07.

coefficient C, captures the variation in entrainment efficiency α encountered (i) across MOSAiC cases ($C = 0.83$), (ii) across prototype cases including sensitivity runs ($C = 0.62$), and (iii) across all cases from all climate regimes combined ($C = 0.91$). Note that the sample size for the prototype group is rather small; it could be further expanded by adding sensitivity experiments at intermediate levels of shear and surface coupling. A benefit of thus linking entrainment efficiency to TKE is that contributions by both shear and buoyancy production are automatically accounted for. Alternative definitions of entrainment rate could thus be thought of that account for shear contributions.

Some spread around this dependence exists, which could be due to physical processes, model shortcomings, numerical effects, and sampling issues. An experimental setting that could affect the results is the spatial discretization, which affects to what degree entrainment is resolved. Previous studies have demonstrated robust representation of Arctic mixed layers at the vertical resolution of 10 m adopted in the lowest few kilometers in this study (Neggers et al. 2019; Rauterkus and Ansorge 2020). However, Mellado (2017) argued that resolving wind shear in strong thermal gradients might require an even higher resolution. Possible physical causes for the remaining spread include the representation of the ice phase in the LES, which is known to have a significant impact on the simulation of Arctic supercooled clouds (e.g., Klein et al.
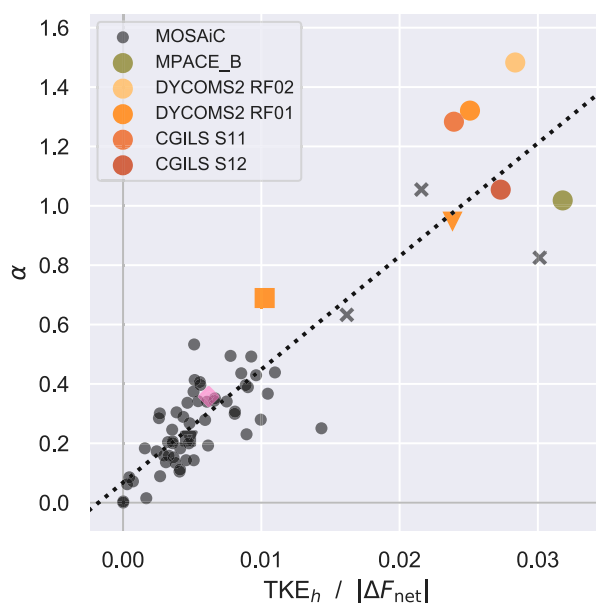
2009; Ovchinnikov et al. 2014; Stevens et al. 2018). Another physical process is the treatment of aerosol in the model (Chylik et al. 2023). In the LES experiments used in this study, the aerosol varies per day, reflecting surface observations (Creamean 2022; Uin and Enekwizu 2024) made during the drift (Schnierstein et al. 2024b). However, the vertical structure of aerosol was simplified. A thorough investigation of these potential impacts on entrainment efficiency is a future research topic.

Concerning sample size, even though 58 cases are a significant step forward from single-case LES studies of Arctic clouds, the question remains to what extent this number guarantees representativity of the Arctic climate. For example, how often do shear-dominated entrainment situations really occur in the high Arctic? Adding cases would further broaden the parameter space of atmospheric conditions and thus represent a more stringent test of the general applicability of the results presented here. To achieve this, one could add MOSAiC simulations initialized at additional radiosonde launch times (at 0500, 1700, and 2300 UTC). This computationally significant effort is currently in progress. While this will be helpful, the MOSAiC drift still represents only 1 year. Considering LES experiments based on observational data from other field campaigns in the Arctic in different years would be advisable.

One aspect not yet discussed is the potential impact of absorption of shortwave radiation at cloud top in both the Arctic (Herman and Goody 1976; Herman and Curry 1984) and warmer (Wood 2012) climates. This process affects the mixed-layer energy budget and thus entrainment efficiency. While all

prototype cases are nocturnal, the library of MOSAiC simulations does include a significant number of cases during polar day (see Table 1). The impact of including shortwave absorption on entrainment is investigated in more detail in appendix B. The results suggest that, on average, the shortwave warming is of secondary order of magnitude compared to the longwave cooling and only weakly affects the entrainment heat fluxes for Arctic clouds as found in this study.

5. Conclusions and outlook

In this study, a library of close to 200 daily large-eddy simulation (LES) experiments based on observational data and covering the full MOSAiC drift was used to investigate the entrainment efficiency of radiatively driven cloudy mixed layers (RCMLs) at high latitudes. Efficiency is here defined as the ratio of entrainment warming to the net longwave cooling at cloud top. A dedicated algorithm to detect such RCMLs in an arbitrary profile was designed for this purpose. Cloud mass in the liquid phase is encountered in about one out of three simulated days, in line with observations and previous research. Most RCMLs detected during MOSAiC were decoupled from the surface. The main outcome and conclusions can be summarized as follows:

- Cloud-top radiative cooling dominates the drift-average bulk mixed-layer heat budget but is partially countered by entrainment warming, at efficiencies of about 21%.
- These efficiencies are much lower compared to previous findings for subtropical warm marine stratocumulus and feature a weak seasonal dependence.
- Investigation of turbulence confirms that the entrainment heat flux is tightly related to turbulent kinetic energy (TKE) at the mixed-layer top.
- High entrainment efficiencies in a few outlying MOSAiC cases are found to be predominantly driven by strong wind shear.
- Surface coupling can also boost entrainment efficiency by (i) enhancing the integrated buoyancy production of TKE and (ii) exposing the RCML to the potentially strong mechanical TKE production in the surface layer.

Contrasting subtropical with Arctic conditions proved helpful for obtaining these insights.

The findings listed above are all derived from model realizations, albeit at high resolutions. While we have confidence in the general representativity of these numerical experiments of nature, as documented by Schnierstein et al. (2024b), they will always remain approximations of reality. In that sense, it is imperative to seek observational support for the entrainment efficiencies reported in this study. The rich MOSAiC database offers opportunities to this purpose. In particular, tethered balloon profile measurements of turbulence, clouds, and radiation (e.g., Lonardi et al. 2022; Pilz et al. 2023) could provide the data needed to calculate entrainment efficiency. While this study is exclusively dedicated to the RCML heat budget, the LES library for the MOSAiC drift offers similar opportunities to structurally explore its humidity budget

under a broad range of atmospheric conditions, in particular the effect of specific humidity inversions on liquid cloud persistence and other microphysical processes. Research toward these goals is in progress.

The results on entrainment in Arctic mixed layers reported here could guide the representation of this process in larger-scale models. The efficiencies reported in this study could function as a useful metric for evaluating and constraining existing parameterizations. In addition, the tight link between the entrainment heat flux and TKE could also provide a way forward for improving new parameterizations, motivating a direct coupling of the parameterized E_h to a realistic subgrid TKE model that includes all important budget terms. The library of LES simulations during MOSAiC could be used as a reference for testing such parameterizations.

Given the predominantly low entrainment efficiencies found for the MOSAiC drift, it is tempting to speculate what this implies for (i) the effective cooling rate of warm, cloudy air masses that enter the Arctic (Pithan et al. 2018) and (ii) the various feedback mechanisms that are known to control Arctic amplification (Serreze and Barry 2011). Entrainment mixing affects the lapse rate in the lower atmosphere, affects the liquid cloud life cycle, and thus affects the energy budget of both the atmosphere and the surface (e.g., Fridlind et al. 2012; Shupe et al. 2013; Solomon et al. 2014). Accordingly, how the lower atmosphere effectively entrains could play a role in how the Arctic climate system responds to perturbations in the rapidly warming climate. Taking one step further, one speculates if some of the known climate sensitivities among models in the Arctic region could be explained by the representation of subgrid-scale entrainment. This is a future research topic that could be inspired by the outcome of this study.

Data availability statement. The configuration files and output data of all LES experiments used in this study are publicly available online as a Zenodo archive (Schnierstein et al. 2024a).

APPENDIX A

RCML Detection Algorithm

Figure A1a illustrates the functioning of the algorithm to detect RCMLs in the LES output, as described in section 2c(1). The MOSAiC case of 7 March 2020 already documented in Fig. 1 is again used as an example. The algorithm is applied at each model output time step (here 300 s). Step (i) is the detection of the height of the strongest net radiative cooling z_{rad}. Step (ii) is the detection of the heights of the five strongest thermal inversions in the profile $z_{\theta_{li}}$, and step (iii) is the calculation of their depths. In step (iv), the inversion height closest to z_{rad} is identified, while steps (v) and (vi) detect the position of the closest mixed layer and cloud layer. On this day, two liquid cloud layers were present.

What stands out is that the five strongest thermal gradients (i) occur throughout the profile, (ii) are not necessarily associated with a cloud layer, and (iii) can jump discontinuously.

Only the inversion closest to z_{rad} evolves gradually and is not discontinuous. Tracking the correct inversion through time is important for investigating the entrainment rate of an RCML, as it reflects the deepening rate of a mixed layer. Figure A1b shows the properties of the RCML selected for this case (green shading), as well as the associated thermal inversion height z_i (solid red) and depth (shaded red), and cloud layer (blue).

Sensitivity tests to the algorithm thresholds listed in Table 2 across ranges applicable to Arctic mixed layers and typical LES time integration steps reveal only minimal impact (not shown).

APPENDIX B

Including Shortwave Absorption

Figure B1 shows the impact of including the shortwave component in the radiative flux jump F_{rad} on the scatterplot expressing entrainment efficiency (as shown before in Fig. 7). Only MOSAiC cases are shown. For cases with nonzero shortwave absorption (polar day), the data point shifts toward the left in the diagram. The shortwave warming can be significant during polar day compared to the net longwave cooling. However, it is
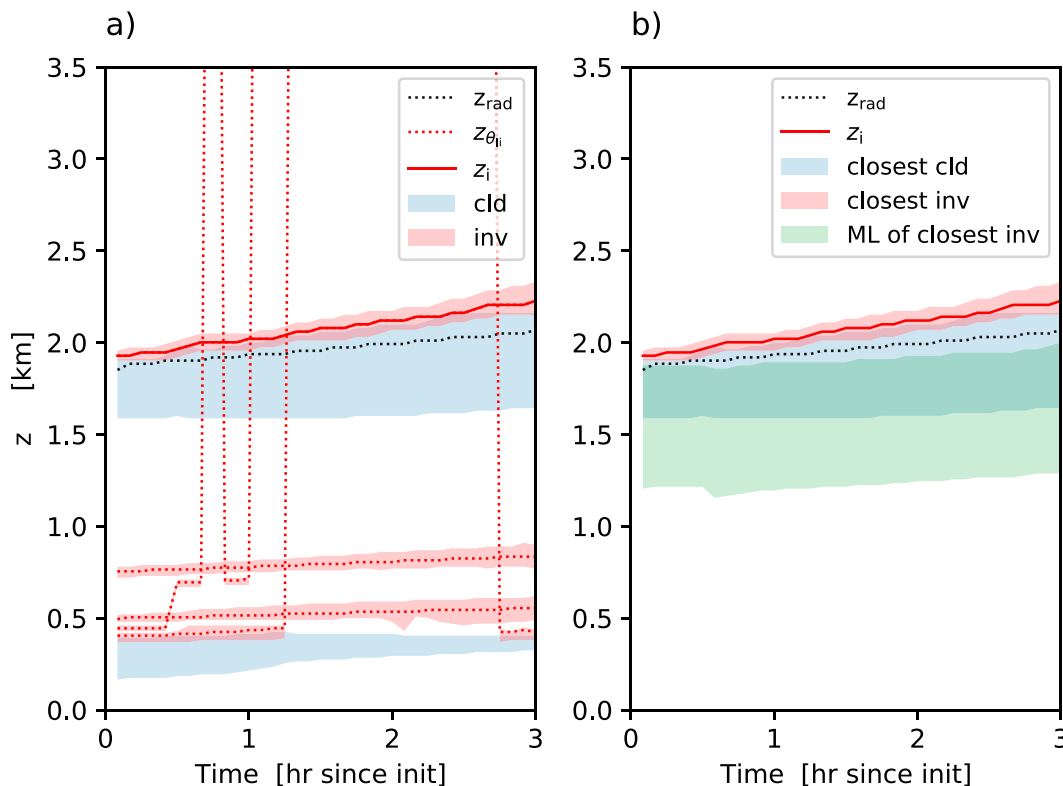

FIG. A1. Time series of the various heights and layers identified by the mixed-layer detection algorithm on 7 Mar 2020. Cloud, inversion, and MLs are indicated by the blue, red, and green shading, respectively. The term z_{rad} is the level with the strongest net LW radiative flux jump (dotted black), while z_i is the thermal inversion height closest to this level (solid red). (a) All liquid cloud (shaded blue) and thermal inversion layers (shaded red) identified in the profile, with $z_{\theta_{li}}$ being the inversion height (dotted red) associated with each detected inversion layer. (b) Only the layers closest to z_{rad}.
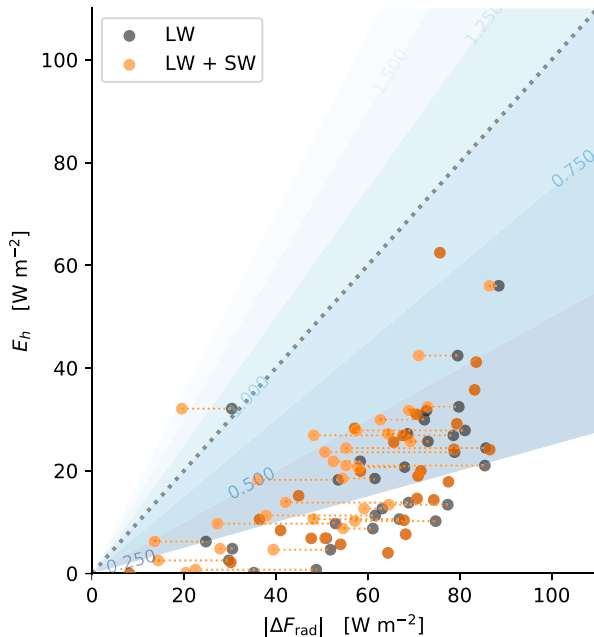
FIG. B1. As in Fig. 7, but now documenting the impact of including the SW component in the radiative flux jump across the cloud layer ΔF_{rad} (orange). These data are connected to the black data points indicating the net LW flux jump for the same case. Brown markers indicate overlapping orange and black data points. Blue background shading indicates the entrainment efficiency α field, for reference (values labeled).

always substantially smaller in magnitude, with the exception perhaps toward small net longwave cooling rates where the relative impact is more significant. However, on average, the entrainment efficiency α (the ratio of the abscissa to ordinate) is not strongly affected and stays well below 1 (the diagonal) for most cases. We conclude from this result that the shortwave impact is on average only of second-order magnitude and does not significantly alter the main results of this study.

REFERENCES

Ackerman, A. S., and Coauthors, 2009: Large-eddy simulations of a drizzling, stratocumulus-topped marine boundary layer. *Mon. Wea. Rev.*, **137**, 1083–1110, https://doi.org/10.1175/2008MWR2582.1.

Bennartz, R., and Coauthors, 2013: July 2012 Greenland melt extent enhanced by low-level liquid clouds. *Nature*, **496**, 83–86, https://doi.org/10.1038/nature12002.

Bretherton, C. S., and M. C. Wyant, 1997: Moisture transport, lower-tropospheric stability, and decoupling of cloud-topped boundary layers. *J. Atmos. Sci.*, **54**, 148–167, https://doi.org/10.1175/1520-0469(1997)054<0148:MTLTSA>2.0.CO;2.

——, and P. N. Blossey, 2014: Low cloud reduction in a greenhouse-warmed climate: Results from Lagrangian LES of a subtropical marine cloudiness transition. *J. Adv. Model. Earth Syst.*, **6**, 91–114, https://doi.org/10.1002/2013MS000250.

Brooks, I. M., and Coauthors, 2017: The turbulent structure of the Arctic summer boundary layer during the Arctic summer cloud-ocean study. *J. Geophys. Res. Atmos.*, **122**, 9685–9704, https://doi.org/10.1002/2017JD027234.

Brost, R. A., J. C. Wyngaard, and D. H. Lenschow, 1982: Marine stratocumulus layers. Part II: Turbulence budgets. *J. Atmos. Sci.*, **39**, 818–836, https://doi.org/10.1175/1520-0469(1982)039<0818:MSLPIT>2.0.CO;2.

Chylik, J., D. Chechin, R. Dupuy, B. S. Kulla, C. Lüpkes, S. Mertes, M. Mech, and R. A. J. Neggers, 2023: Aerosol impacts on the entrainment efficiency of Arctic mixed-phase convection in a simulated air mass over open water. *Atmos. Chem. Phys.*, **23**, 4903–4929, https://doi.org/10.5194/acp-23-4903-2023.

Cox, C., and Coauthors, 2023: Met City meteorological and surface flux measurements (Level 3 Final), Multidisciplinary Drifting Observatory for the Study of Arctic Climate (MOSAiC), central Arctic, October 2019–September 2020. *Arctic Data Center*, https://doi.org/10.18739/A2PV6B83F.

Creamean, J., 2022: Arctic ice nucleation sampling during mosaic. ARM, https://doi.org/10.5439/1798162.

Curry, J. A., 1986: Interactions among turbulence, radiation and microphysics in Arctic stratus clouds. *J. Atmos. Sci.*, **43**, 90–106, https://doi.org/10.1175/1520-0469(1986)043<0090:IATRAM>2.0.CO;2.

——, E. E. Ebert, and G. F. Herman, 1988: Mean and turbulence structure of the summertime Arctic cloudy boundary layer. *Quart. J. Roy. Meteor. Soc.*, **114**, 715–746, https://doi.org/10.1002/qj.49711448109.

Dahlke, S., M. D. Shupe, C. J. Cox, I. M. Brooks, B. Blomquist, and P. Persson, 2023: Extended radiosonde profiles 2019/09-2020/10 during MOSAiC Legs PS122/1 - PS122/5. PANGAEA, https://doi.org/10.1594/PANGAEA.961881.

Day, J., and Coauthors, 2024: The Year of Polar Prediction site Model Intercomparison Project (YOPPsiteMIP) phase 1: Project overview and Arctic winter forecast evaluation. *Geosci. Model Dev.*, **17**, 5511–5543, https://doi.org/10.5194/gmd-17-5511-2024.

de Boer, G., H. Morrison, M. D. Shupe, and R. Hildner, 2011: Evidence of liquid dependent ice nucleation in high-latitude stratiform clouds from surface remote sensors. *Geophys. Res. Lett.*, **38**, L01803, https://doi.org/10.1029/2010GL046016.

Dedekind, Z., U. Proske, S. Ferrachat, U. Lohmann, and D. Neubauer, 2024: Simulating the seeder–feeder impacts on cloud ice and precipitation over the Alps. *Atmos. Chem. Phys.*, **24**, 5389–5404, https://doi.org/10.5194/acp-24-5389-2024.

Devasthale, A., M. Tjernstrom, and A. H. Omar, 2011: The vertical distribution of thin features over the Arctic analysed from CALIPSO observations: Part II: Aerosols. *Tellus*, **63B**, 86–95, https://doi.org/10.1111/j.1600-0889.2010.00517.x.

Driedonks, A. G. M., and P. G. Duynkerke, 1989: Current problems in the stratocumulus-topped atmospheric boundary layer. *Bound.-Layer Meteor.*, **46**, 275–303, https://doi.org/10.1007/BF00120843.

Egerer, U., A. Ehrlich, M. Gottschalk, H. Griesche, R. A. J. Neggers, H. Siebert, and M. Wendisch, 2021: Case study of a humidity layer above Arctic stratocumulus and potential turbulent coupling with the cloud top. *Atmos. Chem. Phys.*, **21**, 6347–6364, https://doi.org/10.5194/acp-21-6347-2021.

Fernández-González, S., F. Valero, J. L. Sánchez, E. Gascón, L. López, E. García-Ortega, and A. Merino, 2015: Analysis of a seeder-feeder and freezing drizzle event. *J. Geophys. Res. Atmos.*, **120**, 3984–3999, https://doi.org/10.1002/2014JD022916.

Fridlind, A. M., B. van Diedenhoven, A. S. Ackerman, A. Avramov, A. Mrowiec, H. Morrison, P. Zuidema, and M. D. Shupe, 2012:

A fire-ACE/SHEBA case study of mixed-phase Arctic boundary layer clouds: Entrainment rate limitations on rapid primary ice nucleation processes. *J. Atmos. Sci.*, **69**, 365–389, https://doi.org/10.1175/JAS-D-11-052.1.

Haghshenas, A., and J. P. Mellado, 2019: Characterization of wind-shear effects on entrainment in a convective boundary layer. *J. Fluid Mech.*, **858**, 145–183, https://doi.org/10.1017/jfm.2018.761.

Herman, G., and R. Goody, 1976: Formation and persistence of summertime Arctic stratus clouds. *J. Atmos. Sci.*, **33**, 1537–1553, https://doi.org/10.1175/1520-0469(1976)033<1537:FAPOSA>2.0.CO;2.

Herman, G. F., and J. A. Curry, 1984: Observational and theoretical studies of solar radiation in Arctic stratus clouds. *J. Climate Appl. Meteor.*, **23**, 5–24, https://doi.org/10.1175/1520-0450(1984)023<0005:OATSOS>2.0.CO;2.

Heus, T., and Coauthors, 2010: Formulation of the Dutch Atmospheric Large-Eddy Simulation (DALES) and overview of its applications. *Geosci. Model Dev.*, **3**, 415–444, https://doi.org/10.5194/gmd-3-415-2010.

Huang, D., E. Campos, and Y. Liu, 2014: Statistical characteristics of cloud variability. Part 1: Retrieved cloud liquid water path at three ARM sites. *J. Geophys. Res.*, **119**, 10 813–10 828, https://doi.org/10.1002/2014JD022001.

Kazil, J., T. Yamaguchi, and G. Feingold, 2017: Mesoscale organization, entrainment, and the properties of a closed-cell stratocumulus cloud. *J. Adv. Model. Earth Syst.*, **9**, 2214–2229, https://doi.org/10.1002/2017MS001072.

Klein, S. A., and Coauthors, 2009: Intercomparison of model simulations of mixed-phase clouds observed during the ARM MIXED-Phase Arctic Cloud Experiment. I: Single-layer cloud. *Quart. J. Roy. Meteor. Soc.*, **135**, 979–1002, https://doi.org/10.1002/qj.416.

Koontz, A., J. Uin, E. Andrews, O. Enekwizu, C. Hayes, and C. Salwen, 2020: Cloud condensation nuclei particle counter (aosccn2colaavg). Atmospheric Radiation Measurement (ARM) User Facility, https://doi.org/10.5439/1323894.

Kostsov, V. S., A. Kniffka, and D. V. Ionov, 2018: Cloud liquid water path in the sub-Arctic region of Europe as derived from ground-based and space-borne remote observations. *Atmos. Meas. Tech.*, **11**, 5439–5460, https://doi.org/10.5194/amt-11-5439-2018.

Lilly, D. K., 1968: Models of cloud-topped mixed layers under a strong inversion. *Quart. J. Roy. Meteor. Soc.*, **94**, 292–309, https://doi.org/10.1002/qj.49709440106.

Linke, O., and Coauthors, 2023: Constraints on simulated past Arctic amplification and lapse rate feedback from observations. *Atmos. Chem. Phys.*, **23**, 9963–9992, https://doi.org/10.5194/acp-23-9963-2023.

Lonardi, M., and Coauthors, 2022: Tethered balloon-borne profile measurements of atmospheric properties in the cloudy atmospheric boundary layer over the arctic sea ice during mosaic: Overview and first results. *Elem. Sci. Anthropocene*, **10**, 000120, https://doi.org/10.1525/elementa.2021.000120.

Mellado, J. P., 2017: Cloud-top entrainment in stratocumulus clouds. *Annu. Rev. Fluid Mech.*, **49**, 145–169, https://doi.org/10.1146/annurev-fluid-010816-060231.

Miller, N. B., M. D. Shupe, C. J. Cox, V. P. Walden, D. D. Turner, and K. Steffen, 2015: Cloud radiative forcing at summit, Greenland. *J. Climate*, **28**, 6267–6280, https://doi.org/10.1175/JCLI-D-15-0076.1.

Morrison, H., G. de Boer, G. Feingold, J. Harrington, M. D. Shupe, and K. Sulia, 2012: Resilience of persistent Arctic mixed-phase clouds. *Nat. Geosci.*, **5**, 11–17, https://doi.org/10.1038/ngeo1332.

Naakka, T., T. Nygård, and T. Vihma, 2018: Arctic humidity inversions: Climatology and processes. *J. Climate*, **31**, 3765–3787, https://doi.org/10.1175/JCLI-D-17-0497.1.

Neggers, R. A. J., J. Chylik, U. Egerer, H. Griesche, V. Schemann, P. Seifert, H. Siebert, and A. Macke, 2019: Local and remote controls on arctic mixed-layer evolution. *J. Adv. Model. Earth Syst.*, **11**, 2214–2237, https://doi.org/10.1029/2019MS001671.

Nicholls, S., and J. Leighton, 1986: An observational study of the structure of stratiform cloud sheets: Part I. Structure. *Quart. J. Roy. Meteor. Soc.*, **112**, 431–460, https://doi.org/10.1002/qj.49711247209.

Nicolaus, M., and Coauthors, 2022: Overview of the MOSAiC expedition: Snow and sea ice. *Elem. Sci. Anthropocene*, **10**, 000046, https://doi.org/10.1525/elementa.2021.000046.

Ovchinnikov, M., and Coauthors, 2014: Intercomparison of large-eddy simulations of Arctic mixed-phase clouds: Importance of ice size distribution assumptions. *J. Adv. Model. Earth Syst.*, **6**, 223–248, https://doi.org/10.1002/2013MS000282.

Overland, J. E., J. M. Adams, and N. A. Bond, 1997: Regional variation of winter temperatures in the Arctic. *J. Climate*, **10**, 821–837, https://doi.org/10.1175/1520-0442(1997)010<0821:RVOWTI>2.0.CO;2.

Persson, P. O. G., C. W. Fairall, E. L. Andreas, P. S. Guest, and D. K. Perovich, 2002: Measurements near the Atmospheric Surface Flux Group tower at SHEBA: Near-surface conditions and surface energy budget. *J. Geophys. Res.*, **107**, 8045, https://doi.org/10.1029/2000JC000705.

Pilz, C., and Coauthors, 2023: Profile observations of the Arctic atmospheric boundary layer with the BELUGA tethered balloon during mosaic. *Sci. Data*, **10**, 534, https://doi.org/10.1038/s41597-023-02423-5.

Pithan, F., and Coauthors, 2018: Role of air-mass transformations in exchange between the Arctic and mid-latitudes. *Nat. Geosci.*, **11**, 805–812, https://doi.org/10.1038/s41561-018-0234-1.

Rabe, B., and Coauthors, 2022: Overview of the MOSAiC expedition: Physical oceanography. *Elem. Sci. Anthropocene*, **10**, 00062, https://doi.org/10.1525/elementa.2021.00062.

Rantanen, M., A. Y. Karpechko, A. Lipponen, K. Nordling, O. Hyvärinen, K. Ruosteenoja, T. Vihma, and A. Laaksonen, 2022: The Arctic has warmed nearly four times faster than the globe since 1979. *Commun. Earth Environ.*, **3**, 168, https://doi.org/10.1038/s43247-022-00498-3.

Rauterkus, R., and C. Ansorge, 2020: Cloud-top entrainment in mixed-phase stratocumulus and its process-level representation in large-eddy simulation. *J. Atmos. Sci.*, **77**, 4109–4127, https://doi.org/10.1175/JAS-D-19-0221.1.

Schnierstein, N., J. Chylik, M. Shupe, and R. Neggers, 2024a: A year in LES: Standardized daily high-resolution large eddy simulations of the Arctic boundary layer and clouds during the MOSAiC drift. Zenodo, https://doi.org/10.5281/zenodo.10491362.

——, ——, M. D. Shupe, and R. A. J. Neggers, 2024b: Standardized daily high-resolution large-eddy simulations of the Arctic boundary layer and clouds during the complete *MOSAiC* drift. *J. Adv. Model. Earth Syst.*, **16**, e2024MS004296, https://doi.org/10.1029/2024MS004296.

Sedlar, J., and M. Tjernström, 2009: Stratiform cloud—Inversion characterization during the Arctic melt season. *Bound.-Layer Meteor.*, **132**, 455–474, https://doi.org/10.1007/s10546-009-9407-1.

——, and M. D. Shupe, 2014: Characteristic nature of vertical motions observed in Arctic mixed-phase stratocumulus. *Atmos. Chem. Phys.*, **14**, 3461–3478, https://doi.org/10.5194/acp-14-3461-2014.

——, ——, and M. Tjernström, 2012: On the relationship between thermodynamic structure and cloud top, and its climate significance in the Arctic. *J. Climate*, **25**, 2374–2393, https://doi.org/10.1175/JCLI-D-11-00186.1.

Seifert, A., and K. D. Beheng, 2006: A two-moment cloud microphysics parameterization for mixed-phase clouds. Part 1: Model description. *Meteor. Atmos. Phys.*, **92**, 45–66, https://doi.org/10.1007/s00703-005-0112-4.

Serreze, M. C., and R. C. Barry, 2011: Processes and impacts of Arctic amplification: A research synthesis. *Global Planet. Change*, **77**, 85–96, https://doi.org/10.1016/j.gloplacha.2011.03.004.

Shupe, M. D., P. O. G. Persson, I. M. Brooks, M. Tjernström, J. Sedlar, T. Mauritsen, S. Sjogren, and C. Leck, 2013: Cloud and boundary layer interactions over the Arctic sea ice in late summer. *Atmos. Chem. Phys.*, **13**, 9379–9399, https://doi.org/10.5194/acp-13-9379-2013.

——, D. D. Turner, A. Zwink, M. M. Thieman, E. J. Mlawer, and T. Shippert, 2015: Deriving Arctic cloud microphysics at Barrow, Alaska: Algorithms, results, and radiative closure. *J. Appl. Meteor. Climatol.*, **54**, 1675–1689, https://doi.org/10.1175/JAMC-D-15-0054.1.

——, and Coauthors, 2020: Arctic report card 2020: The MOSAiC expedition: A year drifting with the Arctic sea ice. Arctic Rep. Card, 8 pp., https://doi.org/10.25923/9G3V-XH92.

——, and Coauthors, 2022: Overview of the MOSAiC expedition: Atmosphere. *Elem. Sci. Anthropocene*, **10**, 00060, https://doi.org/10.1525/elementa.2021.00060.

Silber, I., A. M. Fridlind, J. Verlinde, A. S. Ackerman, G. V. Cesana, and D. A. Knopf, 2021: The prevalence of precipitation from polar supercooled clouds. *Atmos. Chem. Phys.*, **21**, 3949–3971, https://doi.org/10.5194/acp-21-3949-2021.

Solomon, A., M. D. Shupe, P. O. G. Persson, and H. Morrison, 2011: Moisture and dynamical interactions maintaining decoupled Arctic mixed-phase stratocumulus in the presence of a humidity inversion. *Atmos. Chem. Phys.*, **11**, 10 127–10 148, https://doi.org/10.5194/acp-11-10127-2011.

——, ——, O. Persson, H. Morrison, T. Yamaguchi, P. M. Caldwell, and G. de Boer, 2014: The sensitivity of springtime Arctic mixed-phase stratocumulus clouds to surface-layer and cloud-top inversion-layer moisture sources. *J. Atmos. Sci.*, **71**, 574–595, https://doi.org/10.1175/JAS-D-13-0179.1.

——, and Coauthors, 2023: The winter central Arctic surface energy budget: A model evaluation using observations from the MOSAiC campaign. *Elem. Sci. Anthropocene*, **11**, 00104, https://doi.org/10.1525/elementa.2022.00104.

Stephens, G. L., 1978: Radiation profiles in extended water clouds. II: Parameterization schemes. *J. Atmos. Sci.*, **35**, 2123–2132, https://doi.org/10.1175/1520-0469(1978)035<2123:RPIEWC>2.0.CO;2.

Stevens, B., 2002: Entrainment in stratocumulus-topped mixed layers. *Quart. J. Roy. Meteor. Soc.*, **128**, 2663–2690, https://doi.org/10.1256/qj.01.202.

——, and Coauthors, 2003: Dynamics and chemistry of marine stratocumulus—DYCOMS-II. *Bull. Amer. Meteor. Soc.*, **84**, 579–594, https://doi.org/10.1175/BAMS-84-5-579.

——, and Coauthors, 2005: Evaluation of large-eddy simulations via observations of nocturnal marine stratocumulus. *Mon. Wea. Rev.*, **133**, 1443–1462, https://doi.org/10.1175/MWR2930.1.

Stevens, R. G., and Coauthors, 2018: A model intercomparison of CCN-limited tenuous clouds in the high Arctic. *Atmos. Chem. Phys.*, **18**, 11 041–11 071, https://doi.org/10.5194/acp-18-11041-2018.

Tjernström, M., and R. G. Graversen, 2009: The vertical structure of the lower Arctic troposphere analysed from observations and the ERA-40 reanalysis. *Quart. J. Roy. Meteor. Soc.*, **135**, 431–443, https://doi.org/10.1002/qj.380.

——, G. Svensson, L. Magnusson, I. M. Brooks, J. Prytherch, J. Vüllers, and G. Young, 2021: Central Arctic weather forecasting: Confronting the ECMWF IFS with observations from the Arctic Ocean 2018 expedition. *Quart. J. Roy. Meteor. Soc.*, **147**, 1278–1299, https://doi.org/10.1002/qj.3971.

Uin, J., and O. Enekwizu, 2024: Cloud Condensation Nuclei Particle Counter (CCN) instrument handbook. ARM Tech. Rep. DOE/SC-ARM-TR-168, 15 pp., https://doi.org/10.2172/1251411.

van Laar, T. W., V. Schemann, and R. A. J. Neggers, 2019: Investigating the diurnal evolution of the cloud size distribution of continental cumulus convection using multiday LES. *J. Atmos. Sci.*, **76**, 729–747, https://doi.org/10.1175/JAS-D-18-0084.1.

Wendisch, M., and Coauthors, 2019: The Arctic cloud puzzle: Using ACLOUD/PASCAL multiplatform observations to unravel the role of clouds and aerosol particles in Arctic amplification. *Bull. Amer. Meteor. Soc.*, **100**, 841–871, https://doi.org/10.1175/BAMS-D-18-0072.1.

Wood, R., 2012: Stratocumulus clouds. *Mon. Wea. Rev.*, **140**, 2373–2423, https://doi.org/10.1175/MWR-D-11-00121.1.

Zhang, M., and Coauthors, 2013: CGILS: Results from the first phase of an international project to understand the physical mechanisms of low cloud feedbacks in single column models. *J. Adv. Model. Earth Syst.*, **5**, 826–842, https://doi.org/10.1002/2013MS000246.

Zuidema, P., E. R. Westwater, C. Fairall, and D. Hazen, 2005: Ship-based liquid water path estimates in marine stratocumulus. *J. Geophys. Res.*, **110**, D20206, https://doi.org/10.1029/2005JD005833.